united nations educational, scientific and cultural organization

international atomic energy agency

the
abdus salam
international centre for theoretical physics

SMR/1108 - 18

COURSE ON "MEDITERRANEAN SEA(S) CIRCULATION & ECOSYSTEM FUNCTIONING" 2 - 20 November 1998

Trieste, Italy

"Recent Observations in the Yucatan Channel, and a Novel Estimate of Geostrophy Based on, Adding to Hydrology, Velocity Measurements"

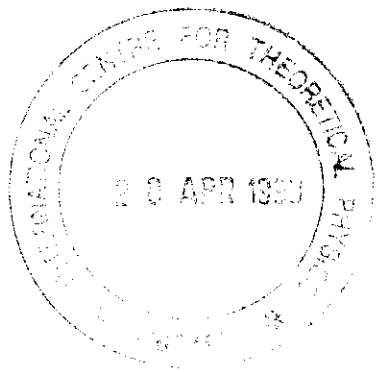

J. OCHOA DE LA TORRE
CICESE
Ensenasda, Mexico

The northern IAS is under the influence of the westerlies in the winter season. The primary synoptic-scale features during the winter are the weekly cold-front passages (*northers* or cold-air outbreaks; Fernandez-Partagas and Mooers, 1975) that penetrate progressively farther south, generate transient shelf circulation, and cool shelf waters (sequentially from the coast to the shelf break) as winter advances. Occasionally, extratropical cyclogenesis occurs near the shelf-break front in the northern IAS, and these cyclones move eastward, generating transient flows and storm surges. Passages of cold fronts are followed by return flows that deliver warm, moist air to the central United States (Lewis and Crisp, 1992). In the summer season, the American Monsoon serves to transport warm, moist air to the central United States; while some of that advection stems from the eastern tropical Pacific, flow (and air–sea transfer) over the IAS is important as well. Historically, the Gulf of Mexico has been a study area for air–sea interaction studies; for example, Price et al. (1978) examined the intermittency of mixed-layer deepening with observations and simulations during both winter and summer storm conditions. [It has also been a study area for transient stratified turbulent bottom boundary layers on a sloping continental shelf (Mercado and Van Leer, 1976; Weatherly and Van Leer, 1977).]

The transit of tropical storms and hurricanes is one of the dominant atmospheric forcing regimes of the Intra-Americas Sea. Typically, four tropical storms reach hurricane intensity in the IAS each year. As Hurricane Gilbert passed through the Cayman Sea (Fig. 7.2; see the color insert), on September 13, 1988, it had a central pressure of 888 mb, the lowest in recent memory; accompanying sustained surface winds were in excess of 82 m s^{-1}, with maximum gusts of 89 m s^{-1} as estimated from the aircraft flight level of 3000 m. As can be seen, the storm affected the entire IAS region, but with localized, high-intensity effects extending to over 100 km from the center. The transient effect of wind stress on the IAS oceanic circulation is one of the many unanswered ques-

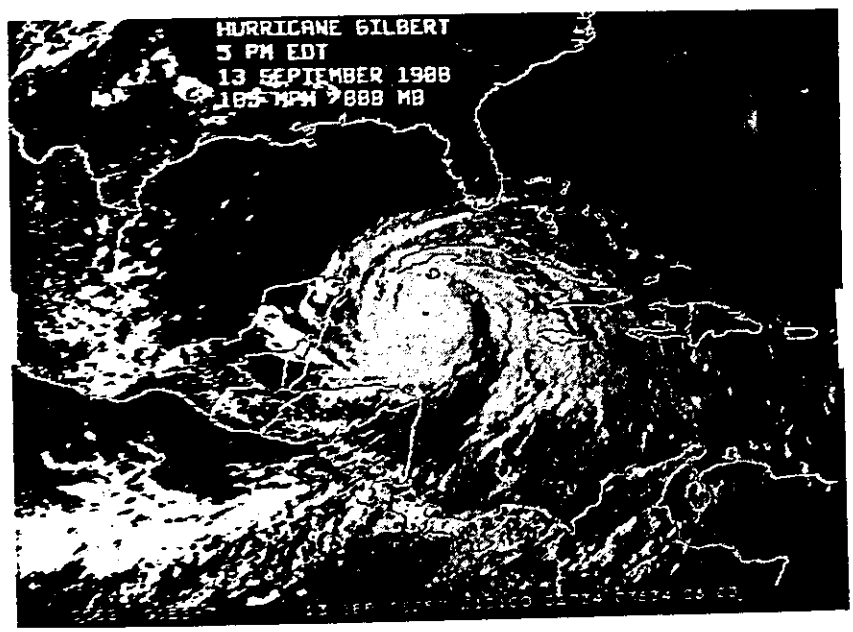

Fig. 7.2. See color insert. Colorized visible image of Hurricane Gilbert. (From NOAA.)

tions about such tropical storms. The surface wind stress from such a storm exceeds 40 dyn cm^{-2} (4 N m^{-2}), or almost two orders of magnitude greater than that from the nominal trade winds. Such a stress would certainly create intensive localized mixing, and its curl would probably produce open ocean upwelling. Its effect on the Gulf of Mexico upper ocean during Hurricane Gilbert (Shay et al., 1992, 1998) was profound, with surface cooling of 3 to 4°C, mixed-layer deepening of 30 to 35 m, strong upwelling and downwelling patterns, downward-propagating near-inertial motions with high vertical shear and an asymmetric wake under the storm track. As long as the region's mangrove forests remain healthy, hurricanes will not particularly exacerbate coastal erosion in undeveloped areas, but for the more populated coasts of the northern IAS and on many islands, these storms significantly affect the shoreline and the coastal ocean.

A changing climate is expected to alter the impact of storms such as Hurricane Gilbert in the IAS. Most especially, a warmer planet could increase both the severity and the frequency of IAS tropical storms (Gray, 1993). While this change may bring more (much needed) rainfall to islands and coasts, it would also produce greater wind damage. Past warm climates (the Holocene optimum of about 6000 years ago and the Eemian of about 125,000 years before the present) suggest that with a warmer global average temperature, the tropical–subtropical IAS may well experience cooler air and SSTs. Lower SSTs would tend to weaken and cause fewer tropical storms and hurricanes according to Gray's (1993) arguments. Thus there is considerable uncertainty as to what changes to anticipate in this mesoscale atmospheric forcing of the IAS with changing global climate, but little uncertainty that the socioeconomic risk is increasing, given the rising human coastal populations.

3. River Runoff Regime

The surface waters of the IAS are influenced by the seasonal runoff from four great rivers: Amazon, Orinoco, Magdelena and Mississippi (Fig. 7.3; see the color insert). (The Magdelena, in the southwestern corner, is the only major river that discharges directly into the Caribbean Sea, and its plume can extend to Jamaica.) Runoff is manifested in buoyant plumes that are important for transporting nutrients, pollutants and freshwater biota over long distances (Muller-Karger et al., 1995; Corredor et al., 1996; Morell et al., 1996). Such plumes are observed as anomalies in ocean color and thermal imagery (Armstrong et al., 1996; Gilbes and Armstrong, 1996) and surface salinity patterns and thus may be used as indicators of surface circulation.

From the temporal dispersion of riverine plumes from satellite observations (Muller-Karger, 1993), the Amazon River Plume most strongly influences the IAS during boreal winter and spring, as during June to January much of its flow is toward Africa in the North Brazil Current retroflection off the Guianas. On the other hand, the Orinoco River plume influences the IAS year round and engulfs the islands of the southern Lesser Antilles and extends across the Caribbean Sea to Puerto Rico. Variability of the discharge in the Mississippi River system is also readily observed in changes of plume size from satellite thermal and visible imagery (Walker, 1996). In most cases, the flow is to the west in the northern Gulf of Mexico (Oey, 1995), but there are instances where the Gulf Loop Current penetrates far enough north that some of the water discharged through the Mississippi Delta, especially under periods of eastward winds, is entrained into the Loop Current and transported into the Straits

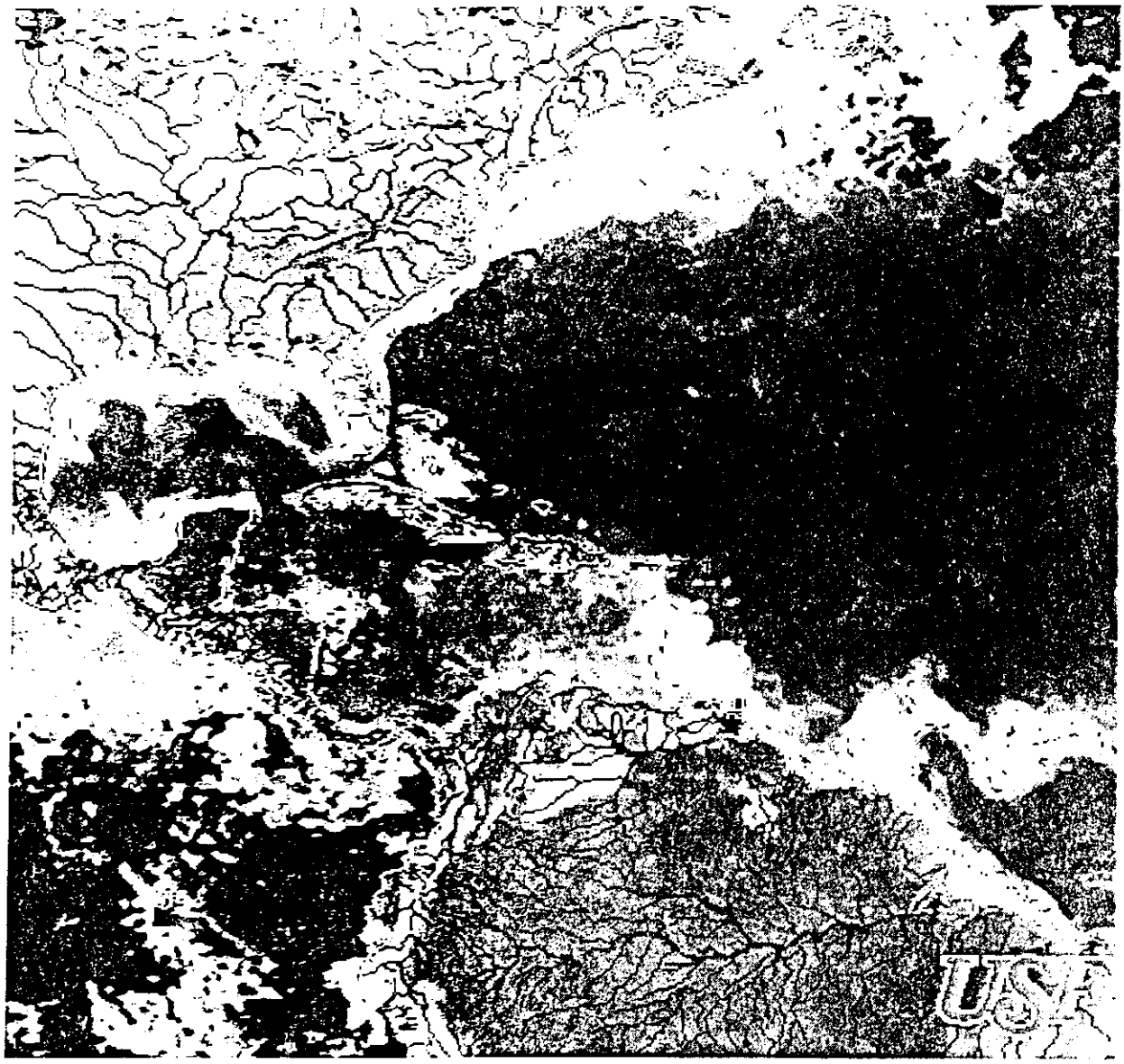

Fig. 7.3. Ocean color image. (From Muller-Karger, 1993.)

of Florida and at least as far north as Georgia (Ortner et al., 1995). Thus the IAS general circulation interacts with river systems in the IAS to carry riverine materials thousands of kilometers from their source.

4. Throughflow Regime

The IAS contains the "roots" of the Gulf Stream system, and its circulation is consequently dominated by throughflow (Figs. 7.4 and 7.5), with a volume transport estimated to be about 30 Sv (Molinari et al., 1985; Schmitz and Richardson, 1991). The inflow is derived from the tropical and subtropical North Atlantic Ocean. For example, the Guyana Current is a major source of inflow from the tropical Atlantic Ocean. The majority of the inflow enters the Caribbean Sea through several passages, of variable sill depth (Kinder et al., 1985; Johns et al., 1996; Wilson and Johns, 1996, 1997), between the Antilles Islands and, to a lesser extent, the Windward Passage (Table I).

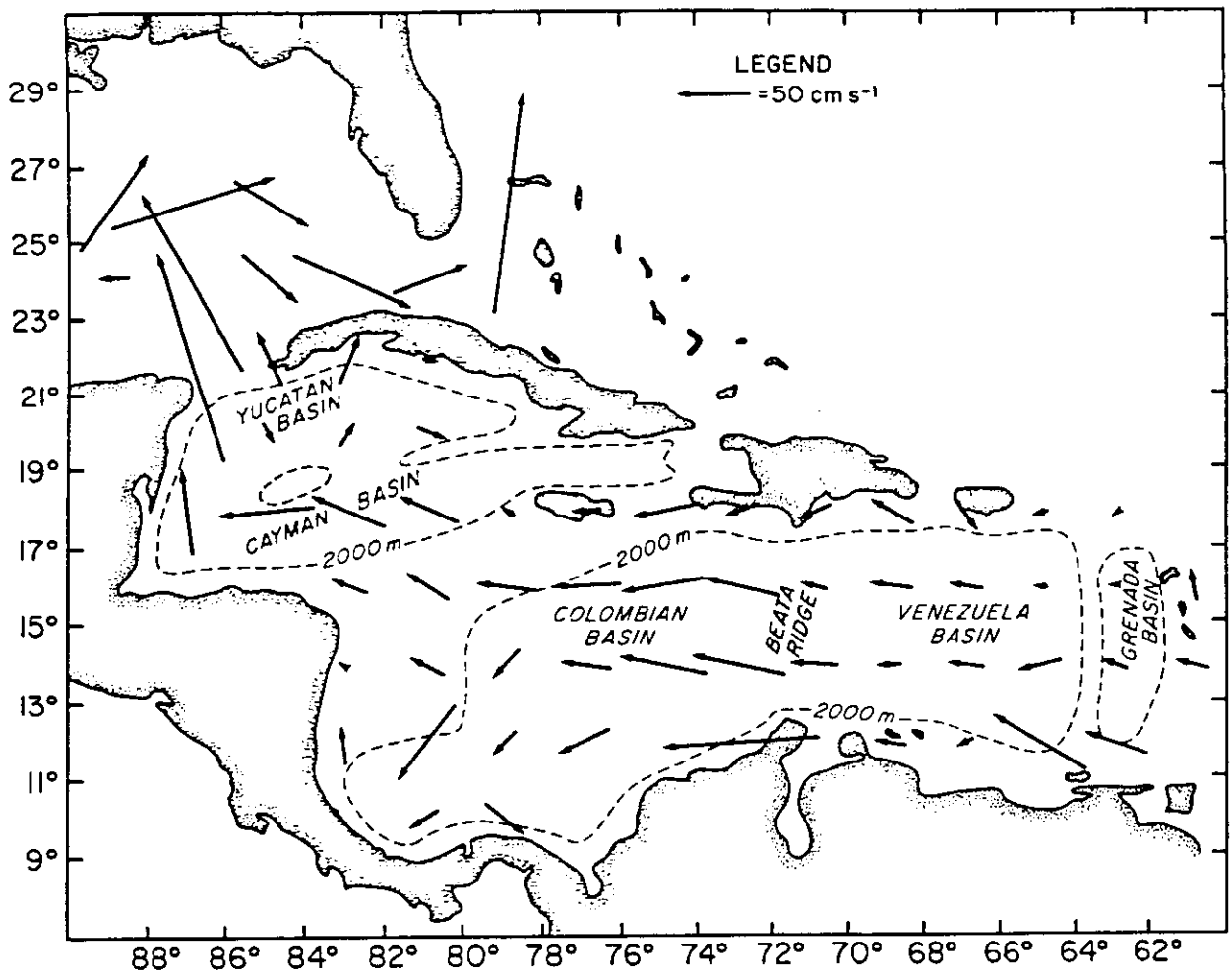

Fig. 7.4. Average surface currents. (From Molinari et al., 1981.)

The remainder bypasses the Caribbean Sea via the Antilles Current, some of which flows through the Bahamas Islands and enters the Straits of Florida. The influence of the climatological mean throughflow on the IAS circulation is modulated by the seasonal cycle and interannual variability of the inflow. Vigorous mesoscale variability, on a two-month time scale, emanating from the tropical and subtropical North Atlantic Ocean, also penetrates the island passages and propagates across the Caribbean Sea (Murphy, 1996).

Associated with the throughflow regime is the thermohaline-driven lower branch of the meridional overturning circulation known as the Deep Western Boundary Current (DWBC), which flows equatorward at a depth of about 3 km along the periphery of the IAS continental slope (Stommel, 1965; Molinari et al., 1992; Lee et al., 1996b). This intense, deep flow is part of the Global Conveyor Belt (Broecker, 1992) in the Atlantic and has a volume transport of about 15 Sv. Although little DWBC water spills directly into the IAS through the major deep passages, it mixes with the ambient middepth Atlantic waters to form the remarkably uniform bottom water in the Caribbean Sea Basin (Wüst, 1964; Gordon, 1967; Roemmich, 1981). Dynamically, the role of the DWBC on IAS circulation is essentially unknown.

The water masses in the IAS are most effectively described from a temperature–

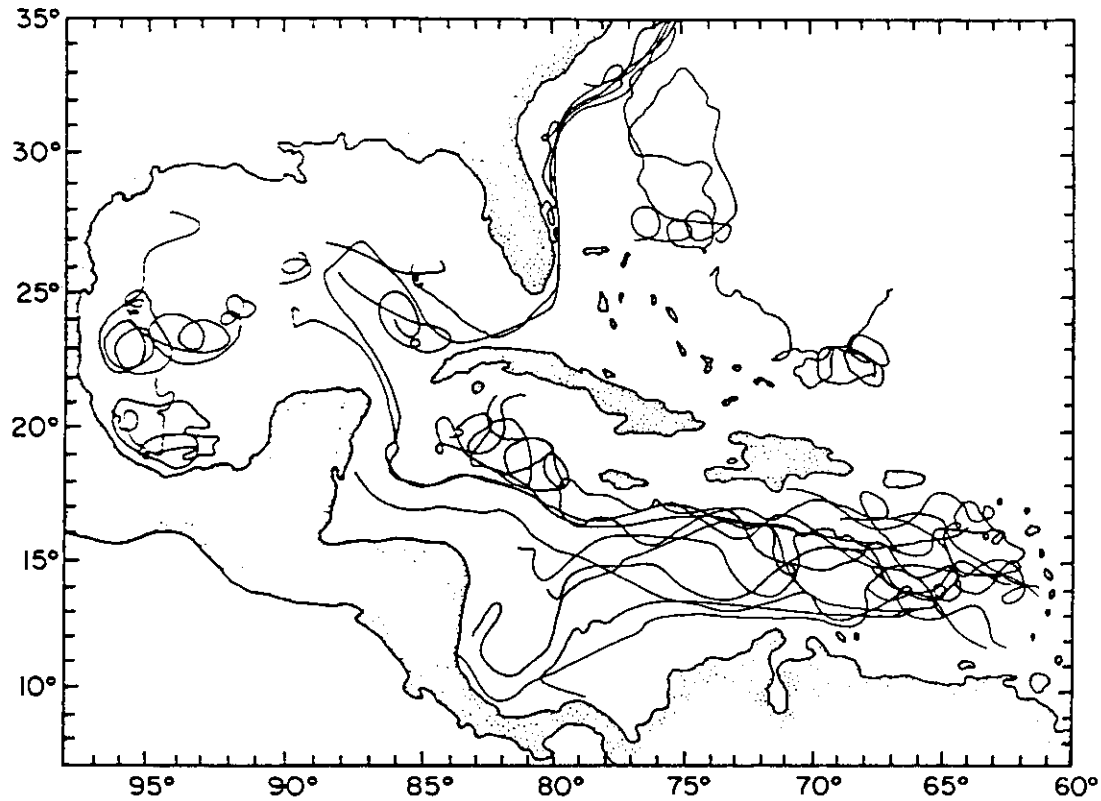

Fig. 7.5. Composite near-surface drifter trajectories. (Composited by G. Maul from various sources.)

salinity (T–S) diagram (Fig. 7.6). Surface waters of the tropical Atlantic Ocean ($T \approx 28$°C, $S \approx 36$ ppt) flow into the IAS through the Antilles Passages, and except for extreme winters, flow out the Straits of Florida with almost the same general T–S properties. Below the surface, at typically 200 m, the subtropical underwater (SUW) dominates the shape of the T–S curve ($T \approx 22$°C, $S \approx 36.7$ ppt) in the main flows of the Gulf Stream system. Outside the current, the salinity is typically reduced to $S \approx 36.2$ ppt, due to mixing with the ambient waters, usually of riverine (R) origin but also due to excess of precipitation (P) over evaporation (E), particularly in the northern Gulf of Mexico. SUW is formed in the central tropical Atlantic where $E > P$ and sinks along isopycnal surface before and during IAS passage.

The next 500 m or so of the water column is dominated by Western North Atlantic Central Water (WNACW) with a typical temperature range of $20°C > T > 8°C$ and salinity range of $36.3 > S > 35.2$ ppt. At about 700 m, the characteristic salinity minimum of Antarctic Intermediate Water (AAIW) near $S \approx 34.8$ ppt and $T \approx 7$°C can be traced from the northern Straits of Florida through the IAS, including the western Gulf of Mexico (where SUW is only found in Loop Current anticyclonic eddies), through the Caribbean Sea and eventually of course to its ($E < P$) source off Antarctica (Wüst, 1964). Finally in the deepest waters, >1000 m or so, the mid-depth waters of the Atlantic (slightly increased salinity) are generally recognized. Not shown in the T–S representation (Fig. 7.6) are the remarkably uniform deep waters of the IAS ($T \approx 4$°C, $S \approx 35$ ppt) created by overflows of the sills in the deeper passages (especially the Anegada and Windward Passages).

One of the remarkable aspects of the T–S correlation in the IAS, and indeed in the Gulf Stream system, is the resiliency of the relationship. Many oceanographers have

TABLE I
IAS Passage Sill Depths and Transport Estimates

Passage (Sv)	Sill Depth (m)[a]	Transport	
		Observed	Modeled[b]
Grenada	740	5.5[c]	4.6
St. Vincent	890	3.3[c]	5.5
St. Lucia	980	1.2[c]	2.0
			1.7
Dominica	950	0.5[c]	1.3
			2.3
Anegada	1915	2.1[c]	3.0
Jungfren	1815		
Mona	475	1.8[c]	3.9
Windward	1560	2.9[d]	2.7
Jamaica	1475		
South Aves	2200		
Yucatán Channel	1900	19.2[d]	26.6
Old Bahama Channel	400	1.9[e]	2.6
Northwest Providence Channel	650	1.2[f]	3.76
Straits of Florida (27°N)	750	32[g]	32.8

[a]Adapted and augmented from Kinder et al. (1985).
[b]Hurlburt and Townsend (1994).
[c]Wilson and Johns (1996, 1997).
[d]Gallegos (1996) upper 1000 m.
[e]Leaman and Molinari (1987).
[f]Leaman et al. (1995).
[g]Larsen (1992) submarine cable.

used the depth of an isotherm to locate water masses (Stommel, 1965). Typically, the 15°C isotherm at 200 m or the 22°C isotherm at 100 m can be used reliably to locate the cyclonic edge of the current (i.e., where $S > 36.5$ ppt). Except in the western Gulf of Mexico, the usual $E - P <$ or $> R$ equation holds well; there the large anticyclonic eddies often inject so much SUW (d) that $E - P = R + d$ best expresses the salt balance. Typical of this mixing are the values near $T \approx 22$°C, $S \approx 36.2$ ppt, where juxtaposed resident Gulf of Mexico waters have mixed with SUW and the 22°C isotherm is typically found at about 50 m depth rather than greater than 100 m in the Gulf Stream system.

5. Climate Regime

With a latitudinal range from the equator at the mouth of the Amazon River to 30°N in the northern Gulf of Mexico (32°N if Bermuda is included biogeographically), the IAS is a tropical–subtropical oceanic regime. Using the Köppen classification scheme, the Greater Antilles and much of the Central American and Guiana coasts are tropical monsoonal in nature; tropical rain forests dominate the Lesser Antilles and coastal southern Colombia, Panama and Costa Rica. Coastal southeastern United States and parts of Mexico are classified as humid subtropical continental climates, but semiarid dry climates are found in eastern Mexico, northern Colombia and Venezuela; parts

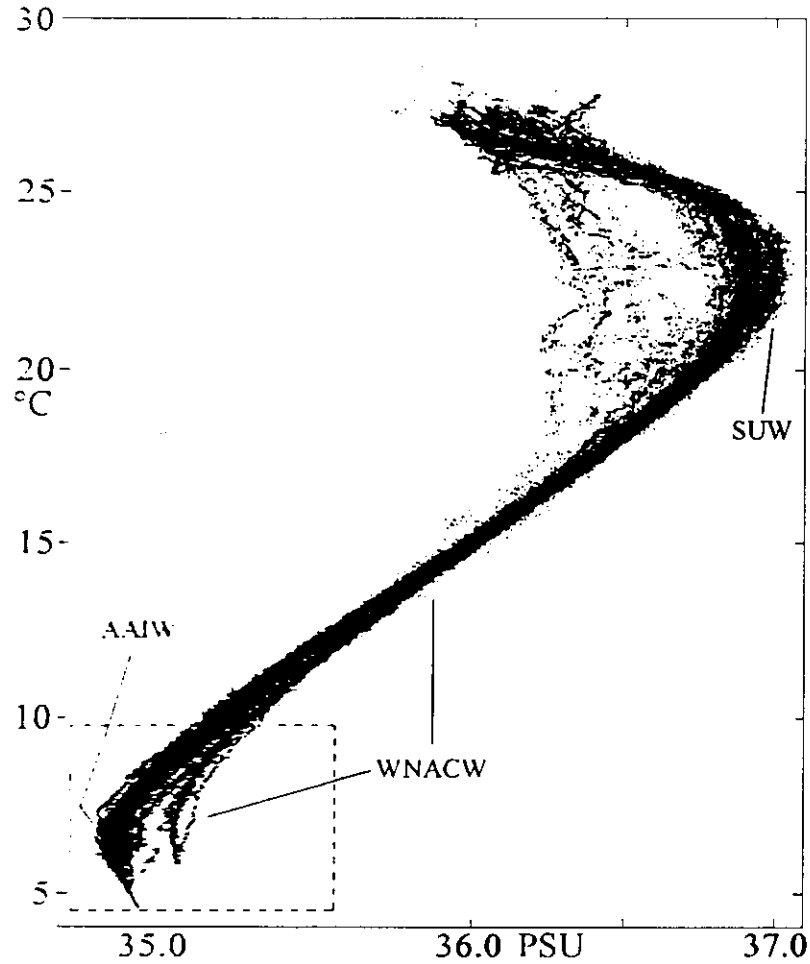

Fig. 7.6. Temperature–salinity diagram. (From Gallegos et al., 1996.)

of the Netherlands Antilles off South America are classified as arid desert. Thus, the coastal IAS has widely varying climatic regimes, with some very localized extremes.

Except for the southern United States, very few long records of IAS temperature, precipitation, sea level or winds are available (Maul, 1993). The longest records, from Key West, Florida, show no statistically significant change in precipitation, although a slight warming of the air has been observed in the past century. Shorter records from Jamaica and Venezuela show more warming than that at Key West, but river runoff changes are not discernible above the nominal interannual variability (Mississippi, Amazon, Orinoco, Magadelena or Rio Grande Rivers; Muller-Karger, 1993). SSTs in the central Caribbean Sea over the last 40 years or so in fact show a slight cooling trend. Sea-level records are all contaminated by land motion and show relative sea level rising as much as 1 cm yr^{-1} off Texas and Louisiana, and falling as much as 0.1 cm yr^{-1} in the tectonically active Lesser Antilles. The best estimate from hydrographic data (0 to 1000 dB) east of the Bahamas is that thermohaline-induced sea-level rise may be as much as 0.15 cm yr^{-1} (Maul and Martin, 1993).

Numerical models of climate change in the IAS all show warming based on the equivalent CO_2 doubling scenario. The SST range increases from 2 to 4°C, depending on the model: computed precipitation changes vary from dryer to wetter and are wholly model dependent [i.e., there is almost no agreement concerning rainfall between the four models considered by Wigley and Santer (1993)]. Sea-level change

has not yet been modeled on the IAS space scale, but if equivalent CO_2-doubling numerical models are used, their inherent positive-feedback nature cannot help but yield thermal warming in the ocean and attendent sea-level rise.

6. General Circulation

The surface flow through the island passages organizes into the Caribbean Current that flows westward off the northern coast of South American and then northward along the eastern coast of Central America (Gordon, 1967; Molinari et al., 1981; Roemmich, 1981; Gallegos, 1996). Subsequently, it becomes known as the Yucatán Current as it flows through the Yucatán Channel and then becomes known as the Loop Current as it penetrates northward into the eastern Gulf of Mexico. It then turns anticyclonically southward to exit to the east through the Straits of Florida, where it is known as the Florida Current and its volume transport is about 30 Sv (Molinari et al., 1985; Schmitz and Richardson, 1991). The persistent cyclonic Panama–Colombian Gyre (PCG), located in the southwestern Caribbean Sea, where it interacts with the plume of the Magdelena River, is the other major component of the surface general circulation.

The flow through the Antillean Passages is spatially complex (i.e., undercurrents and countercurrents: bottom trapping) and temporally variable on time scales of months and years with no clear annual cycle (Wilson and Johns, 1996). As a further example, the flow past Barbados (13.2°N, 59.5°W) exhibits high temporal variability (10-day time scale), topographic steering (anticyclonic sense), and eddy-pair shedding (in von Kármán's sense) in observations and numerical simulations (Bowman et al., 1996).

The deep circulation is largely unexplored but there are dynamical reasons to anticipate a mean cyclonic flow along bottom topography in both the Caribbean Sea and the Gulf of Mexico (Sou et al., 1995). A mean southward flow at the sill (1900 m deep) of the Yucatán Channel of about 0.1 m s^{-1} was observed during a three-year current meter deployment (Maul et al., 1985). Similarly, the ventilation of the deep waters of the Caribbean Sea and Gulf of Mexico is only partially understood (Morrison and Nowlin, 1982; Watlington and Rooth, 1994). The Caribbean Sea is composed of several basins that divide the deep circulation. Geochemical data provide some estimates of deep-water age and residence times (Ribbat et al., 1976; Vesely and Fanning, 1993), but the physical processes involved (e.g., flow over the deep sills of the island passages) are only now being investigated [with the exception of pioneering work of Metcalf (1976)] theoretically and observationally (Rooth and Johns, 1994; MacCready, 1996). Interestingly, in response to wintertime cold-front passages, Gulf of Mexico intermediate water is formed at the shelf break off Texas (Nowlin and Parker, 1974), but the full extent and significance of this process have not yet been determined.

In the western boundary current regime on the eastern side of the Antilles Archipelago, the variability of the Antilles Current and the DWBC dominates the mean flow. Sources of variability include the seasonal cycle (±1.3 Sv, maximum in winter and minimum in autumn) plus westward-propagating mesoscale eddies with a time scale of 70 to 100 days (Lee et al., 1996b). Portions of the DWBC are characterized by recirculation, making observations of met transport and cyclic behavior difficult.

7. Mesoscale Variability

The most dramatic and best known mesoscale variability in the IAS is associated with the anticyclogenesis of the Loop Current, which occurs on time scales of one-half to one-and-a-half years, with a distribution concentrated at 10 to 14 months (Maul and Vukovich, 1993). The anticyclones shed are large (200 to 400 km in diameter), intense (swirl velocities of about 1 m s^{-1}) and durable eddies (lifetimes of several months to a year). The eddies propagate westward at speeds of a few km day^{-1} and interact with bottom topography along the western (and occasionally the northern) Gulf of Mexico, where they generate transient northward (along the western boundary) and eastward (along the northern boundary) shelf–slope flows (see Chapter 6). The eddies interact (through entrainment and detrainment) with shelf waters and dissipate through bifurcation, bottom friction and so on. The anticyclones also induce cyclones over the continental slope and merge with successor eddies. These eddy–topography interactions yield strong upwelling and downwelling velocities deep into the water column with major impacts on marine ecosystems and pollutant transport (Vidal et al., 1994).

Through satellite thermal imagery and numerical simulation, smaller mesoscale cyclonic eddies have been detected along the cyclonic side of the Loop Current. They appear to be generated as the Yucatán Current flows along the eastern coast of the Yucatán Peninsula, probably through onshore advection of cool water in the bottom Ekman layer and subsequent upwelling (Dietrich and Lin, 1994). These cyclonic eddies propagate and grow downstream with the Loop Current; sometimes they stall in the De Soto Canyon (south of Alabama), but more frequently they accumulate off southwest Florida, forming the cyclonic Tortugas Gyre. (Some of these eddies participate in the Loop Current anticyclone pinch-off process by moving westward into the neck of the Loop Current.) On a several-month time scale, the Florida Current meanders offshore and the Tortugas Gyre moves downstream, interacts with shelf waters off the Florida Keys and decays rapidly downstream (Lee et al., 1992, 1994).

While it is well established that the Gulf of Mexico is rich in densely packed mesoscale variability that interacts with shelf water, the mesoscale variability of the Caribbean Sea is less well known (Cabrera et al., 1994). However, there is mounting evidence [through satellite radar altimetry (Nystuen and Andrade, 1993) and numerical simulation (e.g., Murphy, 1996)] that the Caribbean Sea is also rich in mesoscale variability (cf. Kinder et al., 1985). Some of this variability is associated with eddy waves generated by mesoscale features [at least two to three anticyclones per year emanating from the North Brazil Current Retroflection (Johns et al., 1990; Fratantoni et al., 1995; Chapter 8)], and other North Atlantic Ocean eddies (Capella, 1994), impinging on the Antilles island passages; other sources of this variability are meanders of the Caribbean Current (which may be manifestations of the eddy waves induced from the Atlantic) and instabilities of the PCG, which also interact (through entrainment and detrainment) with the meandering Caribbean Current. The PCG consists of an intense cyclone that together with an adjoining anticyclone and cyclone is embedded in a larger but weaker cyclonic gyre. This triad of mesoscale gyres interacts with the shelf waters off Panama, Colombia, Costa Rica and Nicaragua and with the Magdelena River plume. The circulation along the south coast of Cuba is dominated by recurrent gyres, alongshore currents and countercurrents, oceanic fronts and downwelling zones that lead to recirculation and sinking (Díaz et al., 1991). Also,

the southern Cuban shelf has broad, shallow carbonate platforms where evaporative sinking occurs.

8. Wind-Driven Circulation

For shelf circulation, the synoptic-scale events (easterly waves, tropical cyclones and hurricanes in summer, and cold-front passages, return flows and extratropical cyclones in winter) are most significant for driving transient flows. The macroscale, seasonal wind forcing [which is regional as well as remote, i.e., from the North Atlantic (Schmitz et al., 1992), in nature] modulates the general circulation of the open basins by approximately 10% (Larsen, 1992; Maul and Vukovich, 1993) and may lead to flow reversals over shelves. For example, the summertime intensification of the trade winds leads to ecologically significant coastal upwelling and westward shelf flows along the northern coasts of South America (Corredor, 1979; Muller-Karger and Aparicio, 1994), Yucatán Peninsula and Cuba. Recently, ENSO-related variability of the SST in the IAS has been detected (Tourre and White, 1996; Enfield and Mayer, 1997); hence, it can be anticipated that there may be ENSO-related interannual variability in the general circulation as well (cf. Maul, 1993, Chap. 9).

9. Tidal Circulation

The tides and tidal currents of the IAS are relatively weak (less than 1 m and 0.1 m s^{-1}, respectively). Since the northern boundary of the IAS is near the critical latitude for diurnal tides, their spatial structure differs from that of the semidiurnal tides. The IAS encompasses a large region and there are (or have been) numerous tide gauges around the basin; it has proven to be an important regime for observing and modeling tidal phenomena.

Although tides (and their attendant tidal currents) in the IAS are relatively weak, they are complicated. For example, with the form number $F = (K_1 + O_1)/(M_2 + S_2)$, where K_1 and O_1 are the amplitudes of the principal diurnal constituents and M_2 and S_2 are the amplitudes of the principal semidiurnal constituents, F varies considerably within the IAS. As a whole, $F \approx 1$, which characterizes the IAS tide as mixed semidiurnal. However, in the northern Gulf of Mexico and the Venezuelan Basin, $F \geq 3$, which denotes a primarily diurnal tide; in the Cayman Sea and Straits of Florida, $F \leq 0.5$, which is more typical of semidiurnal tides.

Tide gauges in the IAS are used for a variety of purposes, as is common, including vertical surveying datum control, forecasting tides and tidal currents, and measuring relative sea-level change. Because of the many narrow passages, tide gauges have also been shown to be quite well related to the surface currents through the geostrophic relationship $fc = g(\partial h/\partial n)$, where f is the Coriolis parameter, c is the current speed orthogonal to two tide gauges, ∂n is the distance between the gauges, g is gravity, and ∂h is the height difference between the gauges with respect to the geoid. From this approach it has been determined that in the Straits of Florida, there is no statistically significant relationship between the annual cycle of Florida Current surface currents (based on sea-level differences) and the approximate 11-month average shedding of Gulf Loop Current anticyclonic eddies (Maul and Vukovich, 1993). Increasingly, tide gauges are being installed across the passages in the IAS for monitoring and nowcasting geostrophic currents and for control of satellite altimetry.

IAS tide gauges also measure certain catastrophic events, such as storm surge and tsunamis. Currents forced by such episodic events are rather weak overall but locally intense and devastating. The West Indian Hurricane is a well-known feature of the IAS that can produce storm surges as large as 7 m. Equally important, but much less appreciated, is the fact that the IAS, in particular the Caribbean Sea and Bahamas, are vulnerable to seismic sea waves (major events are known to have occurred in 1692, 1755, 1867, 1918 and 1943). In the century or so since the massive Virgin Islands tsunami of 1867, the coastal population in the IAS has increased at least 10-fold, setting the stage for an unprecedented potential loss of life. However, the IOC Tsunami Warning Network has yet to be extended to the IAS (Maul, 1996, Chap. 6).

10. Circulation Modeling

Because of its limited size, the fascination with Loop Current anticyclogenesis and the hazard that mesoscale eddies represent to offshore oil platforms, the Gulf of Mexico has attracted numerous numerical simulation studies and field campaigns. However, the pioneering efforts (Hurlburt and Thompson, 1980) had limited success, due to their neglect of interactions with the Caribbean Sea. The latest generation of models (e.g., Sturges et al., 1993; Oey, 1996) that have incorporated at least a portion of the Caribbean Sea to encompass the variable transport through the Yucatán Channel, if not the entire IAS, have enjoyed more success. In particular, numerical simulations for the entire IAS (Murphy, 1996), consistent with satellite radar altimetric maps of sea surface height (Nystuen and Andrade, 1993), indicate that anticyclones separate from the North Brazil Current Retroflection a few times per year, propagate to the Lesser Antilles, interact with the island passages and induce anticyclones and cyclones in the Caribbean Sea. The anticyclones propagate to the western boundary of the Caribbean and then turn northward with the Caribbean Current, pass through the Yucatán Channel, and enter into the middle of the Loop Current, playing a role in about half of the anticyclonic eddy-shedding events. The cyclones also propagate to the western boundary of the Caribbean Sea, but along a track to the south of the anticyclones, and then turn southward to merge with the PCG. These results indicate mesoscale teleconnections operating throughout the IAS that may have profound consequences for the IAS ecosystem and pollutant transports, as well as for observational and modeling strategies. Nonetheless, there are serious scientific issues (oceanographic, dynamical and numerical) that remain unsettled associated with setting open boundary conditions, whether in the Caribbean Sea or the North Atlantic.

As an example of a contemporary IAS circulation model, several results from IAS-POM [POM, Princeton Ocean Model (Blumberg and Mellor, 1987)] are introduced. IAS-POM is a primitive equation, sigma (terrain-following), free surface, split-mode (external and internal), finite-difference model rendered on an Arakawa C-grid (Ko and Mooers, 1994). It has been implemented preliminarily [with realistic (DBDB5) bottom topography (Levitus 1982), temperature and salinity climatology (Mellor and Yamada, 1982), level $2\frac{1}{2}$ vertical turbulence closure, and Smagorinsky (1963) lateral turbulence closure (with the turbulence parameter (HORCON) equal to 0.05)] on a 20 $\times$ 20 km grid and with 15 vertical (sigma) levels. The forcing is provided by a specified volume transport of 47 Sv on the inflow and outflow boundaries (32 Sv and 15 Sv from the Florida and Antilles Currents, respectively) and Hellerman–Rosenstein (1983) climatological mean surface wind stress.

Based on a 1500-day integration (during which three Loop Current anticyclonic eddies were shed: Gao and Mooers, 1996; Mooers and Gao, 1996), major features of the general circulation and mesoscale variability are revealed (Fig. 7.7): the Caribbean, Yucatán, Loop, Florida and Antilles (which is dominated by mesoscale variability) Currents, plus a Loop Current anticyclonic eddy propagating southwestward, the Tortugas Cyclonic Gyre, and the PCG, which actually consists of a closely packed cyclone–anticyclone–cyclone triad, best detected at depth compared to the surface (Fig. 7.8) but yet to be validated by observations. However, an independent numerical simulation (Hurlburt and Townsend, 1994), with a quite different model and implementation, produced a PCG (Fig. 7.9) with two embedded cyclones at the surface, as did IAS-POM. Based on this integration, six of 20 surface particle trajectories (calculated for 830 days from the simulated currents and a subgridscale turbulent dispersion model) released from the same point in the PCG over the course of a day escaped the Caribbean Sea and experienced widely different fates (Fig. 7.10*a*; see the color insert). [The other 14 particles (not shown) remained in the Caribbean Sea.] One was entrained into a Loop Current anticyclone, another (after orbiting the PCG) was ultimately entrained in a subsequent Loop Current anticyclone, one was entrained into the Tortugas Cyclonic Gyre, one escaped the model domain through the Straits of Florida, and two others also entered the Straits. Similarly, 25 surface particles were released simultaneously at one point just to the northwest of Trinidad to emulate the results of Molinari et al. (1981). Twenty-three of these particles exited the Caribbean Sea through the Yucatán Channel, and the other two became entrained in recirculation zones of the Caribbean Sea (Fig. 7.10*b*).

11. Marine Ecosystems, Fisheries and Pollution Factors

The IAS supports numerous coastal marine ecosystems (Cowen and Castro, 1994), including commercially and recreationally valuable fisheries. The coastal habitats comprise numerous coral reefs, seagrass beds, mangrove forests, coastal lagoons and estuaries (Maul, 1993). The IAS also supports intense offshore oil and gas recovery operations and heavy tanker and other ship traffic. The circulation of the IAS serves to connect the various ecosystems and fisheries through the physical transport and dispersion of fish eggs and larvae; it also provides the physical transport and dispersion for pollutants and ship-generated waste throughout the region. The IAS is clearly a candidate for the Large Marine Ecosystem (LME) approach to understanding interactions of organisms and their oceanic environment (Sherman, 1993). Certainly, the environmental management strategy of the future will need to incorporate the LME interconnectedness of the IAS (Richards and Bohnsack, 1990).

Central to these issues is the need for nowcasts and short-term (ca. 1 week) forecasts of the IAS surface currents and upwelling intensity. For example, marine transportation in the IAS is characterized by heavily trafficked shipping lanes associated with the Panama Canal, the Straits of Florida and the Windward and Mona Passages. Search-and-rescue operations are affected significantly by the lack of detailed knowledge of Gulf Stream–strength surface currents when collision, disabled-vessel, or person-overboard incidents occur. It is this same forecast technology delivery system that is essential to mitigation (and in some cases prevention) of petrochemical spills or jettisoned hazardous cargo.

Pollution in the IAS is pervasive and has both distributed and point sources. The

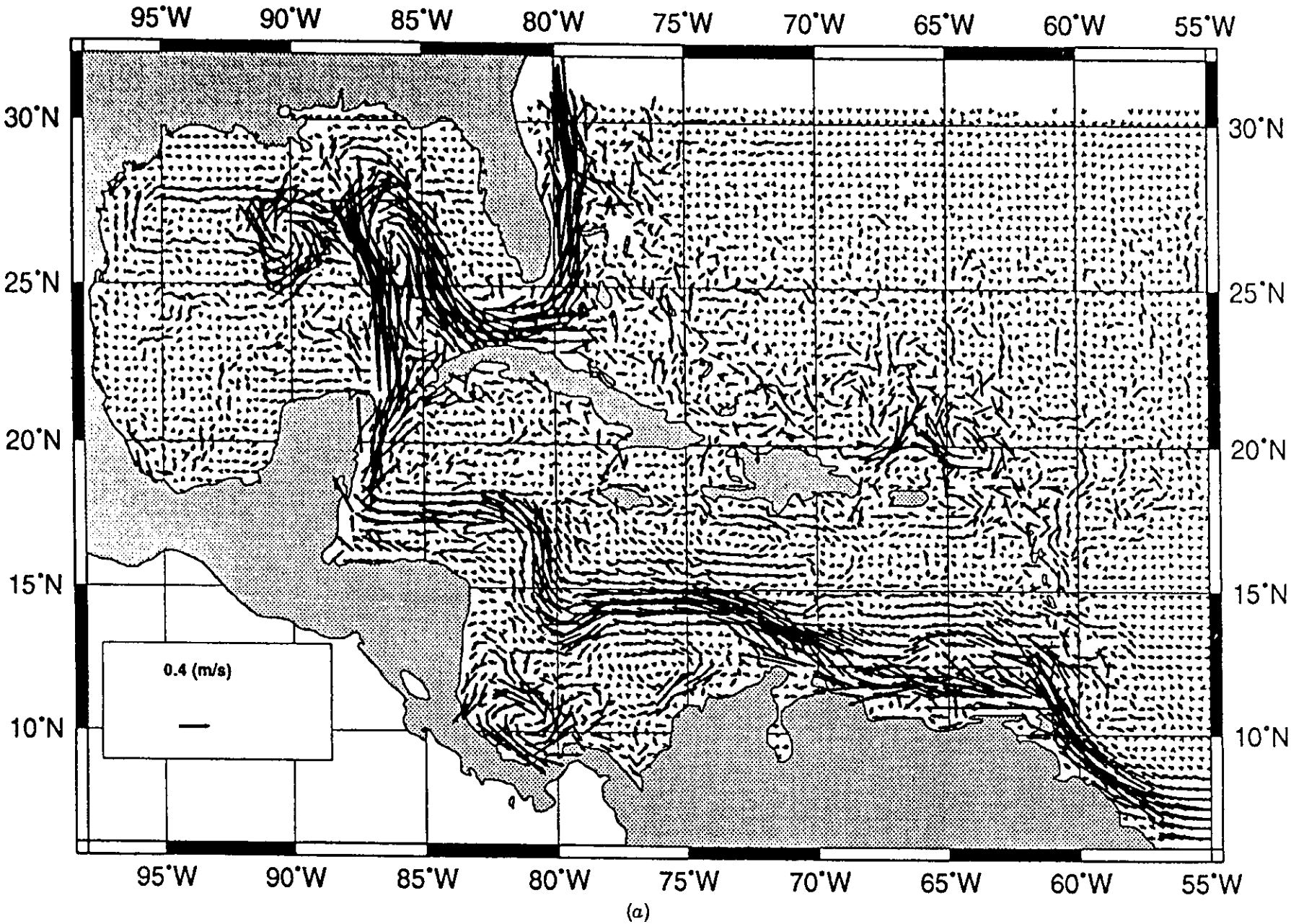

Fig. 7.7. Surface currents from IAS-POM: (*a*) day 1200; (*b*) day 1270.

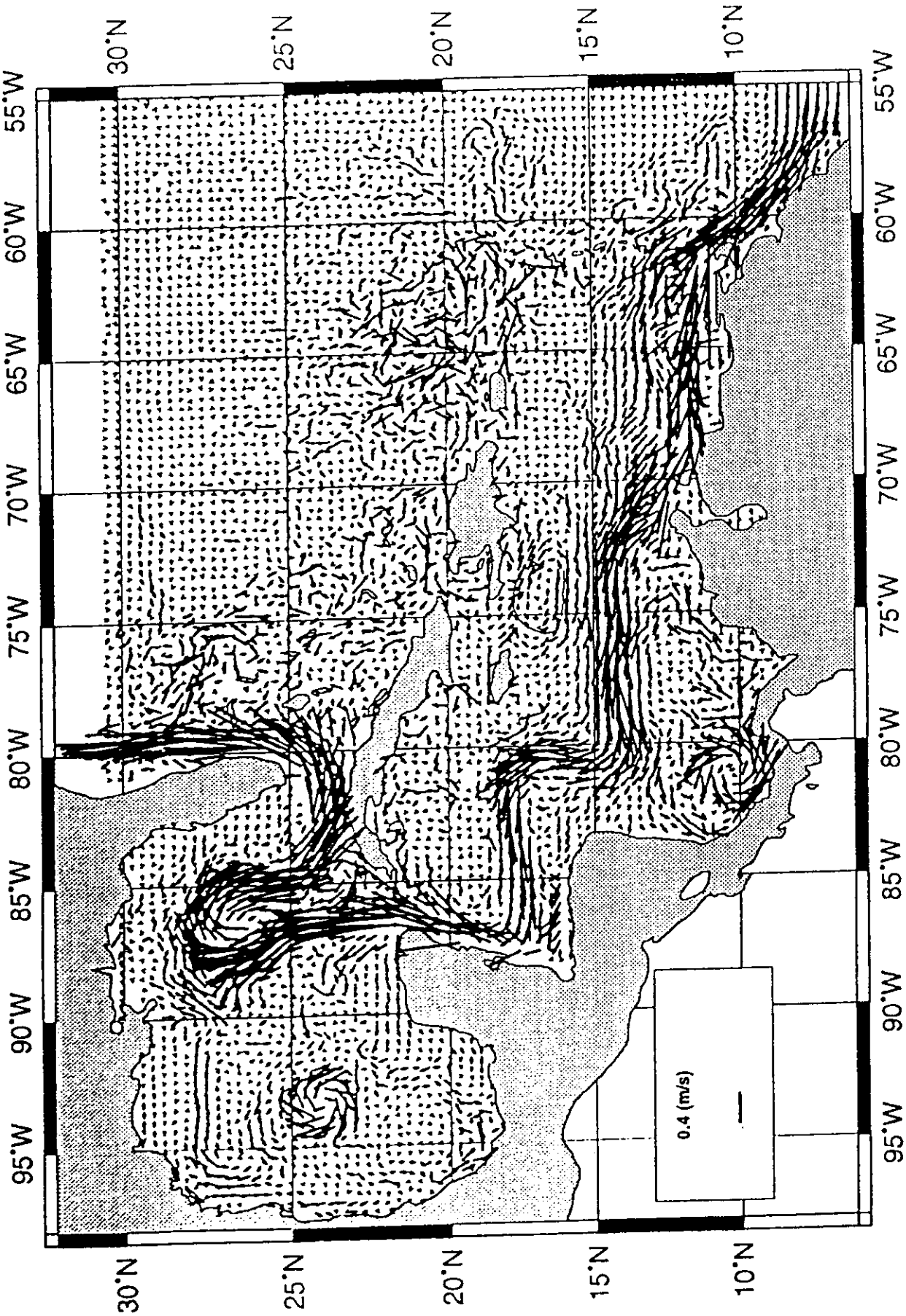

(b)

Fig. 7.7. (*Continued*)

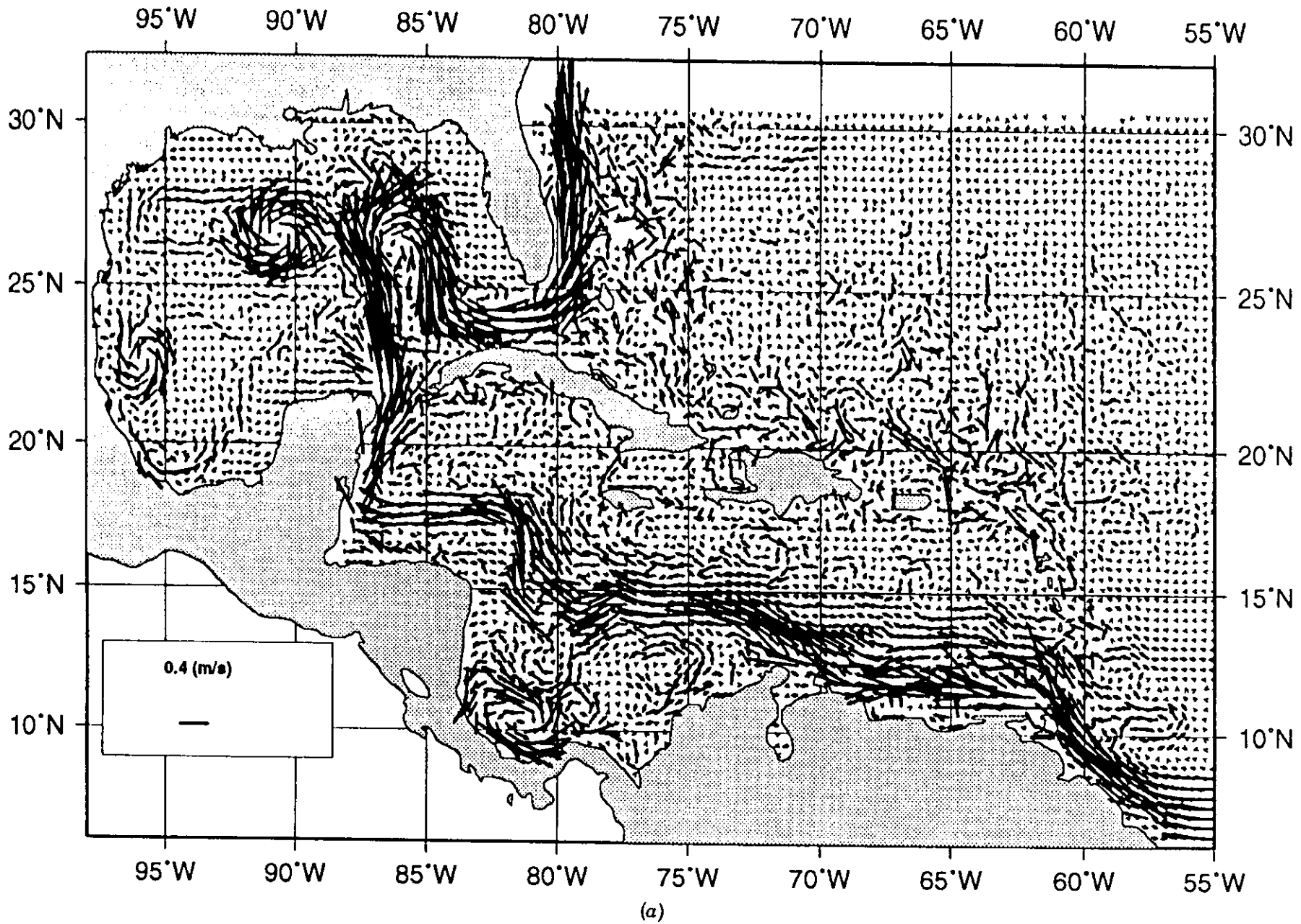

Fig. 7.8. Currents from IAS-POM, day 1350: (*a*) surface; (*b*) 500 m.

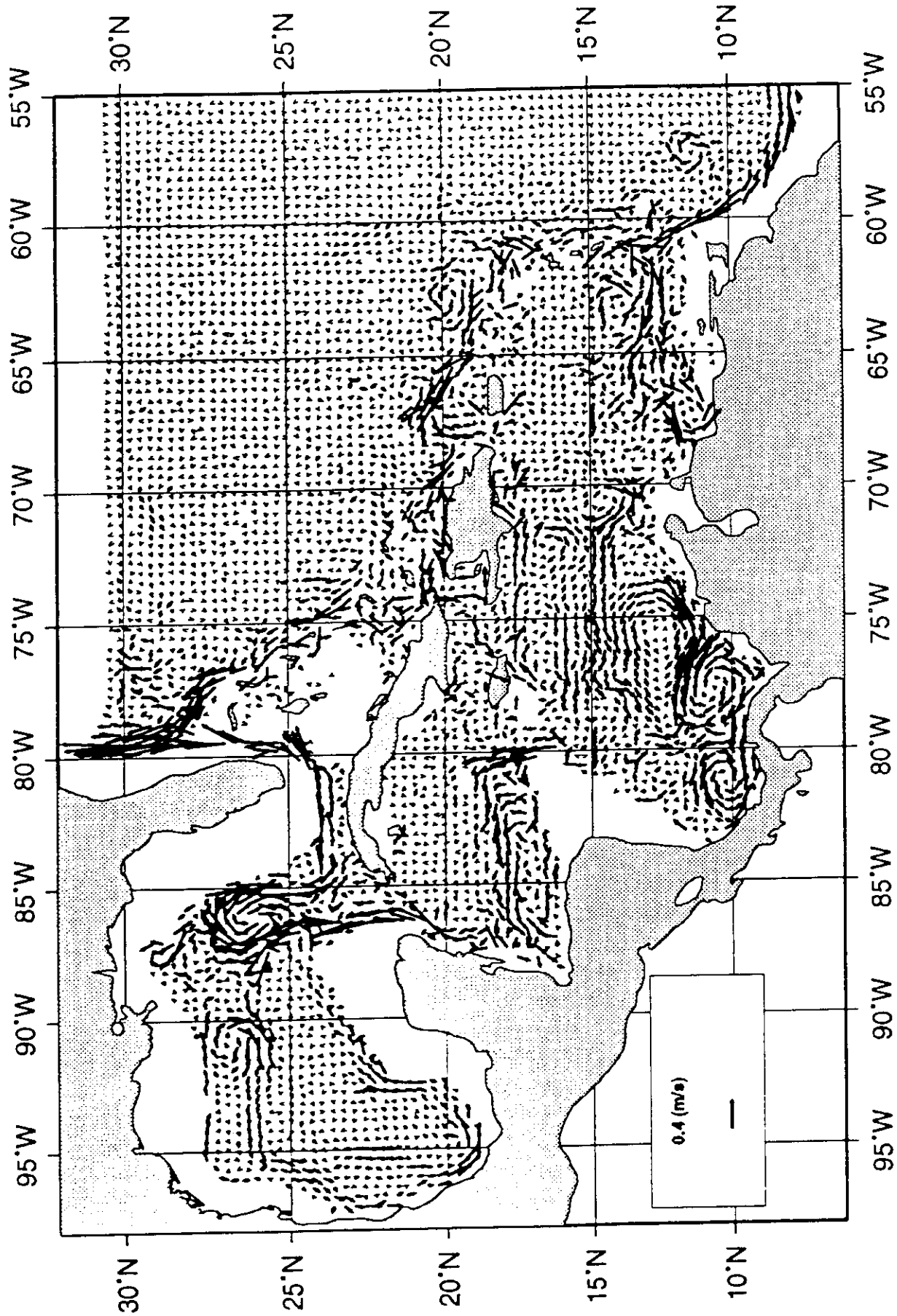

(*b*)

Fig. 7.8. (*Continued*)

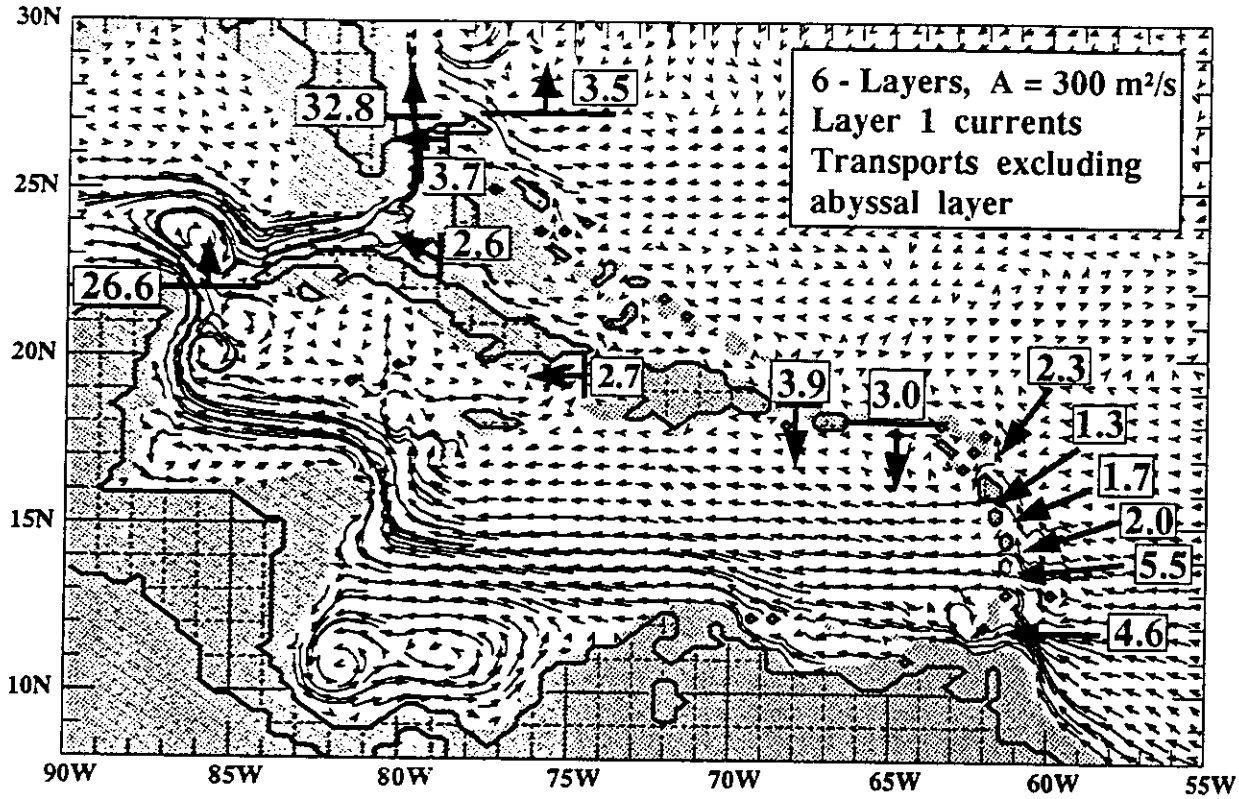

Fig. 7.9. Surface currents. (From Hurlburt and Townsend, 1994.)

many rivers discharging into the region are well known for their role in coastal nutrient enhancement and related impacts on fisheries. Based on spacecraft observations of ocean color (Muller-Karger, 1993), these riverine influences affect coasts many hundreds of kilometers from their respective deltas. More specifically, however, is the issue of petroleum-based coastal environmental impact, beach tar in particular. [In 1995, IMO (the International Maritime Organization of the United Nations) rated the Caribbean Sea as the regional environment having the second-highest (after the Mediterranean Sea) risk due to oil spills.] The eastern shores of many Caribbean islands have significant amounts of tar in their beach sands (Atwood et al., 1987a), as do the beaches of Texas and southeast Florida (Atwood et al., 1987b). Thus, as an impacts issue, the IAS circulation effect on coastal problems is understood, but the need to mitigate catastrophic events by model-based forecasting has largely been unappreciated except in the Straits of Florida (Mooers and Ko, 1994); however, local coastal models for the analysis of oil spill risks are also under development in Colombia and Trinidad.

Forecasts of currents, temperature, salinity and upwelling are also of economic importance for the fisheries of the IAS. Much of the fishing effort is artisanal, particularly in the Caribbean Sea, and it is unclear if local fishermen would (or could) presently use the information. Yet these predictions could improve fisheries management in the interconnected IAS once the scientific understanding of its fish population dynamics is sufficient. In the more developed fisheries of the northern Gulf of Mexico and Straits of Florida, the larger commercial fleets and recreational boats use satellite images and private fishing forecasts to increase the CPUE (catch per unit effort). If however, as in the case of certain New England fisheries, improving the CPUE causes

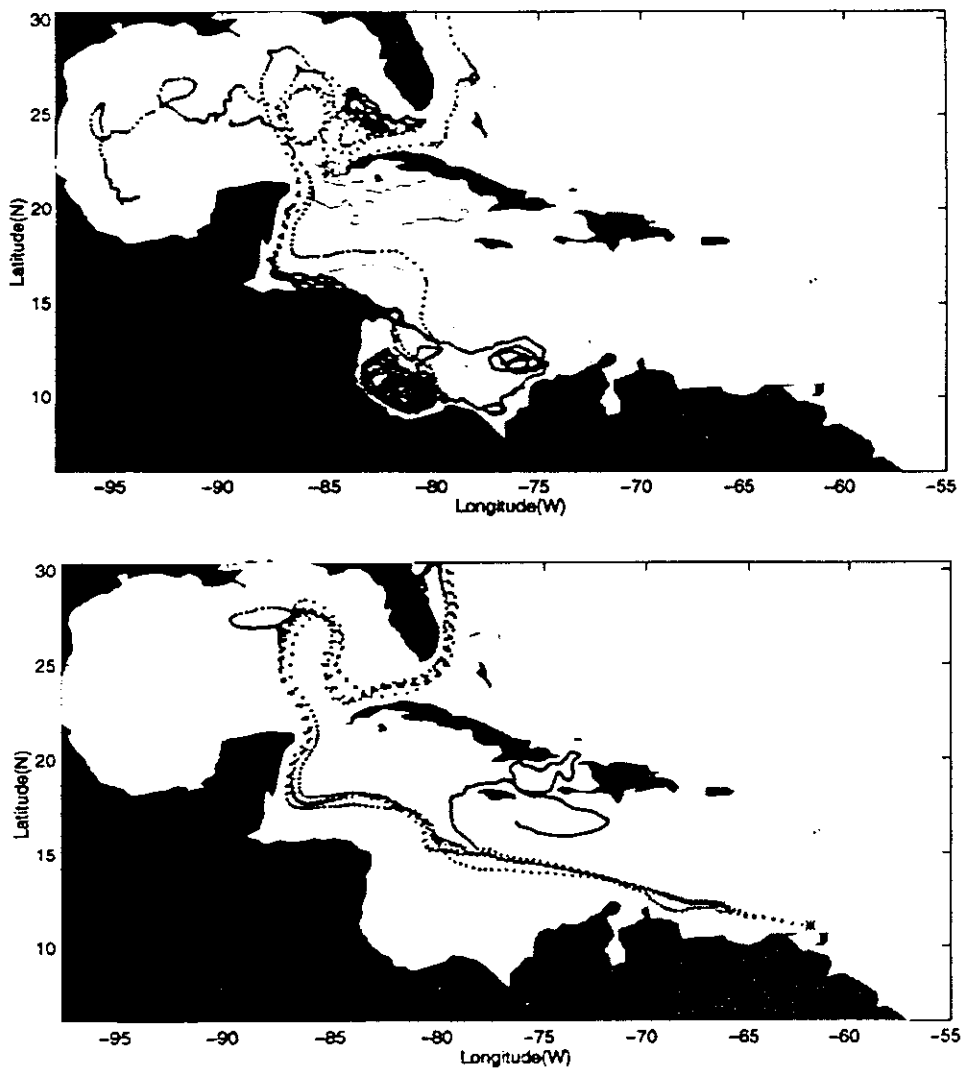

Fig. 7.10. Surface trajectories from IAS-POM: (*a*) release point at 12°N, 82°W, for 830 days (only 6 of 20 trajectories shown); (*b*) release point at 11°N, 62°W, for 490 days (only 8 of 25 trajectories shown).

overfishing, the value added of forecasting currents and upwelling events must link synoptic marine fisheries and environmental management.

12. Summary

The variability of the IAS circulation is well understood on the tidal time scale, but less so on the mesoscale and the seasonal and interannual scales. However, the rapidly increasing knowledge base of the circulation suggests that the IAS is interconnected by physical transports, which, in turn, suggests that societally important issues associated with coastal marine ecosystems, fisheries and pollutants can and should now begin to be addressed on the scale of the IAS. Similarly, societally important scientific issues of regional short-term climate variability (e.g., interannual variations

in precipitation over the central United States due to variable atmospheric moisture flux, in part due to space-time variations in the SST of the IAS) beg further investigation.

Other outstanding research topics include the mechanisms, sites, and rates of ventilation of the deep basins; the transport and exchange through the various island passages; the flow around islands; the interaction of mesoscale features with continental margins; the variability and impact of the regional upwelling phenomena; the impact of the discharge of large rivers on regional ecosystems; and the oceanic teleconnections provided by mesoscale eddy waves emanating from the tropical and subtropical North Atlantic Ocean, which may play important triggering roles for circulation events throughout the IAS. The evolving knowledge of the circulation elements (e.g., recirculation features, dispersal mechanisms, upwelling and downwelling zones and events, retention zones, and space and time scales of mesoscale variability) needs to be translated into Lagrangian transport estimates for the benefit of marine ecosystems and fisheries studies and a host of practical applications for marine management (e.g., ocean pollution, safety at sea, marine transportation and fisheries).

Modern direct current measurements, both Eulerian and Lagrangian, have only been made for the Louisiana, Texas, West Florida and East Florida Shelves in a fairly comprehensive fashion. Elsewhere in the IAS coastal ocean, there is a dearth of lengthy direct current measurements. At this stage of ocean science, it should be possible to apply process knowledge acquired elsewhere to the IAS coastal ocean. However, there will need to be a campaign based on numerical simulations of circulation for the IAS coastal ocean that is well grounded in field observations for model validation. The potential emergence of a regional GOOS (global ocean observing system) for the IAS would not only serve climate variability and change studies but would also serve the development and evaluation of data-assimilative, predictive circulation models. Such modeling systems would be used to advance the knowledge of the IAS coastal ocean circulation, as well as serve pragmatic purposes.

Acknowledgments

Constructive comments provided by William E. Johns, Elizabeth Johns, Thomas N. Lee, Lynn K. Shay, Victor Vidal, Artemio Gallegos, and CDR Carlos Andrade, CN, as well as by anonymous reviewers, are highly appreciated. Lianmei Gao assisted with the IAS-POM calculations and several of the figures. Support from ONR and NOAA is also gratefully acknowledged.

References

Armstrong, R. A., J. M. Morell, J. E. Corredor and J. M. Lopez, 1996. Remote sensing reflectance of eastern Caribbean waters influenced by the Orinoco River plume. *Trans. Am. Geophys. Union*, **76**, 0S 118, Suppl. (abstract only).

Atwood, D. K., F. J. Burton, J. E. Corredor, G. R. Harvey, A. J. Mata-Jimenez, A. Vasquez-Botello and B. A. Walsh, 1987a. Results of the Caripol petroleum pollution monitoring project in the Wider Caribbean. *Mar. Pollut. Bull.*, **18**, 540–548.

Atwood, D. K., S. Dinkel-McKay and G. C. Romero, 1987b. Floating tar and dissolved/dispersed

petroleum hydrocarbons in the northern Gulf of Mexico and the Straits of Florida. *Caribb. J. Sci.*, **23**, 73–76.

Blumberg, A. F. and G. L. Mellor. 1987. A description of a three-dimensional coastal ocean circulation model. In *Three-Dimensional Coastal Ocean Models*, N. S. Heaps, ed. Coastal and Estuarine Sciences 4. American Geophysical Union, Washington, D.C., pp. 1–16.

Bowman, M. J., D. E. Dietrich and C. A. Lin, 1996. Observations and modeling of mesoscale ocean circulation near a small island. In *Small Islands: Marine Science and Sustainable Development*, G. A. Maul, ed. Coastal and Estuarine Studies 51. American Geophysical Union, Washington, D.C., pp. 18–35.

Broecker, W. S., 1992. The Great Ocean Conveyor. In *Global Warming: Physics and Facts*, B. G. Levi, D. Hafemeister, and R. Schribner, eds. American Institute of Physics, New York, pp. 129–161.

Cabrera, E., C. Rooth, W. Johns and M. C. Donoso, 1994. Mesoscale oceanographic characteristics of the Colombian Caribbean sub-basin. *Trans. Am. Geophys. Union*, **74**, 208, Suppl. (abstract only).

Capella, J. E., 1994. Model simulations of Tropical Atlantic mesoscale eddies impinging on the southeastern Caribbean Antilles. *Trans. Am. Geophys. Union*, **74**, 66, Suppl. (abstract only).

CICAR (Cooperative Investigation of the Caribbean and Adjacent Regions) II, 1978. *Symposium on Progress in Marine Research in the Caribbean and Adjacent Regions*. FAO Rep. 200, Suppl. Food and Agricultural Organization of the United Nations, Rome, 638 pp.

Corredor, J. E., 1979. Phytoplankton response to low level nutrient enrichment through upwelling in the Colombian Caribbean Basin. *Deep-Sea Res.*, **26A**, 731–741.

Corredor, J. E., J. M. Morell, R. A. Armstrong and J. M. Lopez, 1996. Influence of the Orinoco River plume on mixed layer features of the eastern Caribbean. *Trans. Am. Geophys. Union*, **76**, OS 118, Suppl. (abstract only).

Cowen, R. K. and L. R. Castro, 1994. Relation of coral reef fish larval distributions to island scale circulation around Barbados, West Indies. *Bull. Mar. Sci.*, **54**, 228–244.

Díaz, C. G., A. L. Chirno, and J. P. Rodríguez, 1991. Corrientes geostroficas en la zee al sur de Cuba. *Rev. Invest. Mar.*, **12**, 29–38.

Dietrich, D. E. and C. A. Lin, 1994. Numerical studies of eddy shedding in the Gulf of Mexico. *J. Geophys. Res.*, **99**, 7599–7615.

Enfield, D. B. and D. A. Mayer, 1997. Tropical Atlantic SST variability and its relation to El Niño–Southern Oscillation. *J. Geophys. Res.*, **102**, 929–945.

Fernandez-Partagas, J. and C. N. K. Mooers, 1975. A subsynoptic study of winter cold fronts in Florida. *Mon. Weather Rev.*, **103**, 742–744.

Fillenbaum, E. R., T. N. Lee, W. E. Johns and R. J. Zantopp, 1997. Meridional heat transport variability at 26.5°N in the North Atlantic. *J. Phys. Oceanogr.*, **27**, 153–174.

Fratantoni, D. M. and W. E. Johns, 1996. A deep-towed ADCP/CTD instrument package developed for abyssal overflow measurements in the northeastern Caribbean Sea. *J. Atmos. Ocean. Technol.*, **13**, 680–687.

Fratantoni, D. M., W. E. Johns and T. L. Townsend, 1995. Rings of the North Brazil Current: their structure and behavior inferred from observations and a numerical simulation. *J. Geophys. Res.*, **100**, 10633–10654.

Gallegos, A., 1996. Descriptive physical oceanography of the Caribbean Sea. In *Small Islands: Marine Science and Sustainable Development*. G. A. Maul, ed. Coastal and Estuarine Studies 51. American Geophysical Union, Washington, D.C., pp. 36–55.

Gallegos, A., I. Victoria, J. Zavala, M. Fernández and I. Penié, 1996. *Hidrología en los Estrechos del Mar Caribe Occidental*. Parte 2. *Resultados Científicos*. Instituto de Ciencias del Mar y Limnología, Universidad Nacional Autónoma de México, 38 pp.

Gao, L. and C. N. K. Mooers, 1996. Numerical simulation of the Intra-Americas Sea. II. *Trans. Am. Geophys. Union*, **76**, OS 142–143, Suppl. (abstract only).

Gilbes, F. and R. Armstrong, 1996. AVHRR detection of Orinoco River plume waters in the eastern Caribbean. *Trans. Am. Geophys. Union*, **76**, OS 118, Suppl. (abstract only).

Gordon, A. L., 1967. Circulation of the Caribbean Sea. *J. Geophys. Res.*, **72**, 6207–6223.

Gray, C. R., 1993. Regional meteorology and hurricanes. In *Climatic Change in the Intra-Americas Sea*, G. A. Maul, ed. United Nations Environment Programme. Edward Arnold, London. pp. 87–99.

Hellerman, S. and M. Rosenstein, 1983. Normal monthly windstress over the world ocean with error estimates. *J. Phys. Oceanogr.*, **13,** 1093–1104.

Hurlburt, H. E. and J. D. Thompson, 1980. A numerical study of Loop Current intrusions and eddy shedding. *J. Phys. Oceanogr.*, **10,** 1611–1651.

Hurlburt, H. E. and T. L. Townsend, 1994. NRL effort in the North Atlantic. In *Data Assimilation and Model Evaluation Experiments: North Atlantic Basin Preliminary Experiment Plan*, R. C. Willems, ed. Tech. Rep. TR-2/95. University of Southern Mississippi/Center for Ocean and Atmospheric Modelling, Hattiesburg, Miss., pp. 30–35.

IOC, 1988. *English–Spanish Bibliography in Physical Oceanography and Climate for the Caribbean Sea and Adjacent Regions*. IOC/INF-783. Intergovernmental Oceanographic Commission of UNESCO, Paris, 49 pp.

IOC, 1995. *Chapman Conference on the Circulation of the Intra-Americas Sea*. Workshop Rep. 111. Intergovernmental Oceanographic Commission of UNESCO, Paris, 14 pp. + appendices.

Johns, W. E., T. N. Lee, F. A. Schott, R. J. Zantopp and R. H. Evans, 1990. The North Brazil Current retroflection: seasonal structure and eddy variability. *J. Geophys. Res.*, **95,** 22103–22120.

Johns, E., W. D. Wilson and R. L. Molinari, 1996. Transport balance of the Intra-Americas Sea: results from NOAA's Subtropical Atlantic Climate Study. *Trans. Am. Geophys. Union*, **76,** OS 117, Suppl. (abstract only).

Kinder, T. H., G. W. Heburn and A. W. Green, 1985. Some aspects of the Caribbean circulation. *Mar. Geol.*, **68,** 25–52.

Ko, D. S. and C. N. K. Mooers, 1994. A numerical simulation of circulation in the Intra-Americas Sea. *Trans. Am. Geophys. Union*, **74,** 209, Suppl. (abstract only).

Larsen, J. C., 1992. Transport and heat flux of the Florida Current at 27°N derived from cross-stream voltages and profiling data: theory and observations. *Philos. Trans. R. Soc. London Ser A*, **338,** 169–236.

Leaman, K. D. and R. L. Molinari, 1987. Topographic modification of the Florida Current by Little Bahama and Great Bahama Banks. *J. Phys. Oceanogr.*, **17,** 1724–1736.

Leaman, K. D., P. S. Vetes, L. P. Atkinson, T. N. Lee, P. Hamilton and E. Waddell, 1995. Transport, potential vorticity, and current temperature structure across Northwest Providence and Santaren Channels and Florida Current off Cay Sal Bank. *J. Geophys. Res.*, **100,** 8561–8569.

Lee, T. N., C. Rooth, E. Williams, M. F. McGowan, A. Szmant and M. E. Clarke, 1992. Influence of Florida Current, gyres and wind-driven circulation on transport of larvae and recruitment in the Florida Keys coral reefs. *Cont. Shelf Res.*, **12,** 971–1002.

Lee, T. N., M. E. Clarke, E. Williams, A. F. Szmant and T. Berger, 1994. Evolution of the Tortugas Gyre and its influence on recruitment in the Florida Keys. *Bull. Mar. Sci.*, **54,** 621–646.

Lee, T. N., W. E. Johns, R. J. Zantopp and E. R. Fillenbaum, 1996a. Moored observations of western boundary current variability and thermohaline circulation at 26.5°N in the subtropical North Atlantic. *J. Phys. Oceanogr.*, **26,** 962–983.

Lee, T. N., W. E. Johns and R. J. Zantopp, 1996b. Annual and semiannual cycles of meridional transport east of Bahamas at 26.5°N. *Trans. Am. Geophys. Union*, **76,** OS 117, Suppl. (abstract only).

Levitus, S., 1982. *Climatological Atlas of the World Ocean*. NOAA Prof. Pap. 13. National Oceanic and Atmospheric Administration. U.S. Department of Commerce, Rockville, Md., 173 pp.

Lewis, J. M. and C. A. Crisp, 1992. Return flow in the Gulf of Mexico. II. Variability in return-flow thermodynamics inferred from trajectories over the Gulf. *J. Appl. Meteorol.*, **31,** 882–898.

MacCready, P., 1996. Overflow into the deep Caribbean. *Trans. Am. Geophys. Union*, **76,** OS 208, Suppl. (abstract only).

Maul, G. A., ed., 1993. *Climatic Change in the Intra-Americas Sea*. United Nations Environment Programme. Edward Arnold, London, 389 pp.

Maul, G. A., ed., 1996. *Small Islands: Marine Science and Sustainable Development*. Coastal and Estuarine Studies 51. American Geophysical Union. Washington, D.C., 463 pp.

Maul, G. A. and D. M. Martin, 1993. Sea level rise at Key West, 1846–1992: America's longest instrument record? *Geophys. Res. Lett.*, **20,** 1955–1959.

Maul, G. A. and F. M. Vukovich, 1993. The relationship between variations in the Gulf of Mexico Loop Current and Straits of Florida volume transport. *J. Phys. Oceanogr.*, **23,** 785–796.

Maul, G. A., D. A. Mayer and S. R. Baig, 1985. Comparisons between a continuous 3-year current-meter observation at the sill of the Yucatan Strait, satellite measurements of Gulf Loop Current area, and regional sea level. *J. Geophys. Res.*, **90,** 9089–9096.

Mellor, G. L. and T. Yamada, 1982. Development of a turbulence closure model for geophysical fluid problems. *Rev. Geophys. Space Phys.*, **20,** 851–875.

Mercado, A. and J. Van Leer, 1976. Near bottom velocity and temperature profiles observed by cyclesonde. *Geophys. Res. Lett.*, **3,** 633–634. (Erratum, *Geophys. Res. Lett.*, **4,** 96.)

Metcalf, W. G., 1976. Caribbean–Atlantic water exchange through the Anegada–Jungfern Passage. *J. Geophys. Res.*, **81,** 6401–6409.

Molinari, R. L., M. Spillane, I. Brooks, D. Atwood and C. Duckett, 1981. Surface currents in the Caribbean Sea as deduced from Lagrangian observations. *J. Geophys. Res.*, **86,** 6537–6542.

Molinari, R. L., W. D. Wilson and K. Leaman, 1985. Volume and heat transports of the Florida Current: April 1982 through August 1983. *Science*, **227,** 295–297.

Molinari, R. L., R. A. Fine and E. Johns, 1992. The deep western boundary current in the tropical North Atlantic Ocean. *Deep-Sea Res.*, **39,** 1967–1984.

Mooers, C. N. K. and L. Gao, 1996. Numerical simulation of the Intra-Americas Sea. *Trans. Am. Geophys. Union*, **76,** OS 118. Suppl. (abstract only).

Mooers, C. N. K. and D. S. Ko, 1994. Nowcast system development for the Straits of Florida. In *Estuarine and Coastal Modeling III*, M. L. Spaulding, K. Bedford, A. Blumberg, R. Cheng and S. Swanson, eds. American Society of Civil Engineers, New York, pp. 158–171.

Morell, J. M., J. E. Corredor, R. A. Armstrong and J. M. Lopez, 1996. The effects of massive riverine input upon planktonoic respiration in the eastern Caribbean. *Trans. Am. Geophys. Union*, **76,** OS 118, Suppl. (abstract only).

Morrison, J. M. and W. D. Nowlin, Jr., 1982. General distribution of water masses within the eastern Caribbean Sea during the winter of 1972 and fall of 1973. *J. Geophys. Res.*, **87,** 4207–4229.

Muller-Karger, F. E., 1993. River discharge variability including satellite-observed plume-dispersal patterns. In *Climatic Change in the Intra-Americas Sea*, G. A. Maul, ed. United Nations Environment Programme. Edward Arnold, London, pp. 162–192.

Muller-Karger, F. E. and R. Aparicio, 1994. Mesoscale processes affecting phytoplankton abundance in the southern Caribbean Sea. *Cont. Shelf Res.*, **14,** 199–221.

Muller-Karger, F. E., P. L. Richardson, and D. McGillicuddy, 1995. On the offshore dispersal of the Amazon's plume in the North Atlantic. *Deep-Sea Res.*, **42,** 2127–2137.

Murphy, S. J., 1996. The connectivity of eddy variability in the Caribbean Sea, the Gulf of Mexico, and the Atlantic Ocean. Master's thesis, Department of Oceanography, Florida State University, Tallahassee, Fla., 51 numb. leaves.

Nowlin, W. D. and A. Parker, 1974. Effects of a cold-air outbreak on shelf water of the Gulf of Mexico. *J. Phys. Oceanogr.*, **4,** 467–486.

Nystuen, J. A. and C. A. Andrade, 1993. Tracking mesoscale ocean features in the Caribbean Sea using GEOSAT altimetry. *J. Geophys. Res.*, **98,** 8389–8394.

Oey, L.-Y., 1995. Eddy and wind-forced shelf circulation. *J. Geophys. Res.*, **100,** 8621–8637.

Oey, L.-Y., 1996. Simulation of mesoscale variability in the Gulf of Mexico: sensitivity studies, comparison with observations, and trapped wave propagation. *J. Phys. Oceanogr.*, **26,** 145–175.

Ortner, P. B., T. N. Lee, P. J. Milne, R. G. Zika, M. E. Clarke, G. P. Podesta, P. K. Swart, P. A. Tester, L. P. Atkinson and W. R. Johnson, 1995. Mississippi River flood waters reach the Gulf Stream. *J. Geophys. Res.*, **100,** 13595–13602.

Price, J. F., C. N. K. Mooers and J. C. Van Leer, 1978. Observation and simulation of storm-induced mixed-layer deepening. *J. Phys. Oceanogr.*, **8,** 582–599.

Ribbat, B., W. Roether and K. D. Munnich, 1976. Turnover of eastern Caribbean deep water from C-14 measurements. *Earth Planet. Sci. Lett.*, **32,** 331–341.

Richards, W. J. and J. A. Bohnsack, 1990. The Caribbean Sea: a large marine ecosystem in crisis. In

Large Marine Ecosystems: Patterns, Processes, and Yields, K. Sherman, L. M. Alexander, and B. D. Gold, eds. American Association for the Advancement of Science, Publ. 90-30S, Washington, D.C., pp. 44–53.

Roemmich, D., 1981. Circulation of the Caribbean Sea: a well-resolved inverse problem. *J. Geophys. Res.*, **86**, 7993–8005.

Rooth, C. G. and W. E. Johns, 1994. Structure and variability of the sill-controlled flow of North Atlantic Deep Water into the central Caribbean deep basin. *Trans. Am. Geophys. Union*, **75**, 208, Suppl. (abstract only).

Schmitz, W. J., Jr. and P. L. Richardson, 1991. On the sources of the Florida Current. *Deep-Sea Res.*, **38**, S379–S409.

Schmitz, W. J., Jr., J. D. Thompson and J. R. Luyten, 1992. The Sverdrup circulation for the Atlantic along 24°N. *J. Geophys. Res.*, **97**, 7251–7256.

Shay, L. K., P. G. Black, A. J. Mariano, J. D. Hawkins and R. L. Elsberry, 1992. Upper ocean response to Hurricane Gilbert. *J. Geophys. Res.*, **97**, 20227–20248.

Shay, L. K., A. J. Mariano, S. D. Jacob and E. H. Ryan, 1998. Mean and near-inertial ocean current response to Hurricane Gilbert. *J. Phys. Oceanogr.*, **28.**

Sherman, K., 1993. Emerging theoretical basis for monitoring the changing states (health) of large marine ecosystems. *NOAA Tech. Memor. NMFS/F-NEC-100.* National Oceanic and Atmospheric Administration, U.S. Department of Commerce, Rockville, Md., 27 pp.

Smagorinsky, J., 1963. General circulation experiments with the primitive equations. I. The basic experiment. *Mon. Weather Rev.*, **91**, 99–164.

Sou, T., G. Holloway and M. Eby, 1995. Effects of topographic stress on Caribbean Sea circulation. *J. Geophys. Res.*, **101**, 16449–16453.

Stommel, H., 1965. *The Gulf Stream.* University of California Press, Berkeley, Calif., 248 pp.

Sturges, W., J. C. Evans, S. Welsh and W. Holland, 1993. Separation of warm-core rings in the Gulf of Mexico. *J. Phys. Oceanogr.*, **23**, 250–268.

Tourre, Y. M. and W. B. White, 1996. Evolution of the ENSO signal in the Eastern Pacific–Intra-Americas Sea. *Trans. Am. Geophys. Union*, **76**, OS 117, Suppl. (abstract only).

Vesely, E. and K. Fanning, 1993. Silica in the deep Caribbean Sea distribution during three decades. *Proceedings fo the 3rd Meeting of the Oceanography Society* (abstract only).

Vidal, V. M. V., F. V. Vidal, A. F. Hernandez, E. Meza and J. M. Perez-Molero, 1994. Baroclinic flows, transports, and kinematic properties in a cyclonic–anticyclonic–cyclonic ring triad in the Gulf of Mexico. *J. Geophys. Res.*, **99**, 7571–7597.

Walker, N. D., 1996. Satellite assessment of Mississippi River plume variability: causes and predictability. *Remote Sens. Environ.*, **58**, 21–35.

Watlington, R. A. and C. G. H. Rooth, 1994. Turbulent evolution of deep basin stratification. *Trans. Am. Geophys. Union*, **75**, 208, Suppl. (abstract only).

Weatherly, G. L. and J. C. Van Leer, 1977. In *Bottom Turbulence*, J. C. A. Nihoul, ed. Elsevier Oceanography Series 22, Elsevier, Amsterdam, pp. 103–122.

Wigley, T. M. L. and B. D. Santer, 1993. Future climate of the Gulf/Caribbean Basin from Atmospheric general circulation models. In *Climate Change in the Intra-Americas Sea*, G. A. Maul, ed. United Nations Environment Programme, Edward Arnold, London, pp. 31–54.

Wilson, W. D. and W. E. Johns, 1996. Measurements of current structure and transport in the Windward Islands Passages: 1991–1995. *Trans. Am. Geophys. Union*, **76**, OS 117, Suppl. (abstract only).

Wilson, W. D. and W. E. Johns, 1997. Velocity structure and transport in the Windward Islands Passages. *Deep-Sea Res.*, **44**, 487–520.

Wüst, G., 1964. *Stratification and Circulation in the Antillean–Caribbean Basins. I. Spreading and Mixing of the Water Types with an Oceanographic Atlas.* Columbia University Press, New York, 201 pp. + appendices.

This is the file: optimo.rdm
=README file to get the submitted version of

Optimal extraction of the geostrophic contribution
from hydrographic and horizontal velocity sections

by

J. Ochoa, J. Sheinbaum, J. Candela, A. Badan & D. Wilson

Submitted to JMR, sep. '98.

Enter as anonymous user by ftp to our machine

```
ftp canek.cicese.mx
 or
ftp 158.97.14.5
 now
cd dist
bin
 since it is a gzip compressed postcript file,
 includes text and figures.
get optimo.ps.gz
 (you'll find this file, optimo.rdm, too)
 exit from ftp
 check size,
 uncompress w/
gzip -d optimo.ps.gz
 recheck size
 if sizes are OK, you have it
```

To check size(ls -la optimo*) :

```
-rw-r--r--    1 abadan   user      828287 Sep 25 10:20 optimo.ps.gz
-rw-r--r--    1 abadan   user     4535293 Sep 25 10:20 optimo.ps
```

Your comments are welcomed:
jochoa@cicese.mx
or: julios@cicese.mx
or: jcandela@cicese.mx
or: abadan@cicese.mx
or: WILSON@aoml.noaa.gov

Journal of Marine Research, xx, xxx–xxx, 1998

Optimal extraction of the geostrophic contribution from hydrographic and horizontal velocity sections

by J. Ochoa,[1] J. Sheinbaum,[1] J. Candela,[1] A. Badan[1] and D. Wilson[2]

ABSTRACT

It is becoming common practice to measure the horizontal ocean current velocities together with the hydrography by lowering an ADCP on typical CTD casts. The velocities thus observed are considered to consist of a background contribution in geostrophic balance with superposed internal wave anomalies. We present a method to separate the two by minimizing the volume integral of the internal wave energy. This variational approach leads to a Poisson equation for the geostrophic pressure, which is forced by the potential vorticity (PV) inferred from the measurements. As in the geostrophic adjustment problem, the PV is retained in the geostrophic components, so the residual anomalies remain PV free. This method offers a natural choice for the boundary condition, one that optimizes the energy retained in the geostrophic estimate.

As an example, the method is applied to a vertical section across the Yucatan Channel, where we compare the terms in the thermal wind equation to the measured fields, interpolated from observations by objective mapping.

1. Introduction

The relatively recent development of lowering a package consisting of a CTD and an ADCP measuring simultaneously during hydrographic casts has increased substantially the information gathered during an oceanographic expedition, without requiring much additional shiptime. The studies of Wilson and Leetmaa (1988) and Wilson and Johns (1997) are good examples of the vast amount of observations that can be gathered in this fashion and of the important information that can be derived from it. Total horizontal velocities can also be obtained with either accurate positioning of the ship (Wilson, 1994) or by using the capability of the ADCP to determine its own motion when the bottom is within its signal range (Fratantoni and Johns, 1996). Techniques to process ADCP data collected in this way have been developed by Fischer and Visbeck (1993) and Wilson (1994); software can be obtained at www.ldeo.columbia.edu/~visbeck/ladcp.

1. Oceanografía Física, CICESE, Apdo. postal 2732, Ensenada, Mexico
2. NOAA, AOML, Miami, Florida, U.S.A.

Although the instantaneous velocities across an ocean section give us a direct measure of the transports involved, a valid and important inquiry consists of extracting the semipermanent components of the flow and hydrography by separating them from high frequency transients, in the hopes that they represent an important fraction whose evolution can be best predicted by numerical models. Then, this separation becomes nothing but the initialization problem of numerical forecastings, which remains a very modern endeavour, of which a huge publication list can be compiled (Daley, 1991). Another reason to determine the geostrophic fields with high precision is to infer upwelling and downwelling motions in frontal zones (Hoskins *et al.*, 1978; Pollard and Regier, 1992; Pinot *et al.*, 1996; Rudnick, 1996), where internal waves are again high frequency reversible motions that greatly contaminate the net transport signal. Of course, a portion of the semipermanent contributions might not necessarily be in geostrophic balance; for example, Hinrichsen and Lehman (1995) used such CTD/ADCP profiling measurements to show significant ageostrophic shears in Biskayne Bay.

Straightforward attempts to use a reference near-surface velocity measured with a ship-mounted ADCP, at a depth were it is hoped that the influence of non-geostrophic processes is small, and then integrate the thermal wind equation on hydrographic data available at depth were made by Saunders (1992) and Cokelet, Schall and Dougherty (1996). These methods combine hydrographic observations made in the entire water column with shipboard ADCP velocity measurements in only the top 200-300 m of the ocean. A common restriction set in geostrophic velocity estimates based on shipboard ADCP measurements is enforcing nondivergence; for example, Chereskin and Trunnell (1996) usually do so by finding a streamfunction that reproduces the measured vorticity (as in Pollard and Regier, 1992), a practice that occurs even with numerical simulations (Pinot *et al.*, 1996). We share the goal of determining the absolute geostrophic velocity in the water column, but the problem is approached with a more general perspective. To have vertical profiles of velocity for the same water columns for which hydrography is available provides the extra advantage that potential vorticity can be computed. The method proposed here goes one step further from the previous studies above, by adding vertical structure and reproducing the measured potential vorticity. But curiously enough, this conservation law is not the starting point of the method but a consequence.

Our approach is based on the work of Dickiy (1969) and simply answers one question: Given the observed fields of horizontal velocity and density, which geostrophically balanced state is the 'closest' to them? The measure of closeness is shown to be best defined by the energy equation of linearized dynamics, although the density energy is the same for the non-linear case. Rudnick (1996) also proposed the minimization of a quadratic measure which, in fact, reduces to the internal wave energy

when appropriate weights are chosen. Selecting a dynamic quantity (Energy) for the minimization clarifies that it consists simply of extracting the vortical modes from the observations. Rudnick (1996, appendix A) also made the comment that since density is measured with much more accuracy than velocity, the three dimensional Poisson equation that results from his method is poorly conditioned. Using dynamical weights allows to solve the full problem, in which a 'geostrophic density' is also derived (although the example shown here is limited to a two-dimensional case), without the poor conditioning. Whether this will remain true in other cases is unclear.

The Euler-Lagrange equation that results from the variational approach proposed here implies a geostrophic estimate that reproduces the quasi-geostrophic potential vorticity (PV) deduced from the observations. It is well-known that this conservation law can be derived without using a variational formulation, and is the key element in solving the geostrophic adjustment problem (Gill, 1982). The variational principle, however, permits to derive the appropriate boundary conditions for irregular domains and shows explicitly that the extremum is a minimum.

The following section outlines the method, leaving mathematical detail for Appendix A. For completness, Appendix B shows the analogous result for the shallow water equations, directly related to the work of Vallis (1992). The third section shows an application of this method in a section across the Yucatan Channel, with an assessment of how much the thermal wind equation balance is fulfilled by the measurements. Comments and conclusions are given in the fourth section.

2. The Method

Observed horizontal velocity and hydrography are assumed to consist of the superposition of a geostrophic background, plus ageostrophic and measurement noise contributions. The observed fields are $u = u(\mathbf{r})$, $v = v(\mathbf{r})$ and $\rho = \rho(\mathbf{r})$, where u and v are the zonal and meridional velocity components, ρ is mass density and $\mathbf{r} = (x, y, z)$ is the position with cartesian coordinates x to the East, y to the North, and z upwards. The separation in those contributions can be specified by

$$(\rho_o f v,\ -\rho_o f u,\ -g\rho) = \nabla\widetilde{p} + (\rho_o f v',\ -\rho_o f u',\ -g\rho'), \tag{1}$$

where the field $\widetilde{p}$ is the geostrophic pressure, the prime denotes ageostrophic plus noise components, f is the Coriolis parameter, ρ_o is a constant reference density, and g is the gravitational acceleration.

It is not in general expected that the measurements themselves fulfill the requirements for the vector $(\rho_o f v,\ -\rho_o f u,\ -g\rho)$ to have a potential function (i.e. a plausible function $\widetilde{p}$ such that equation (1) holds with $u' = v' = \rho' = 0$), since for this to be possible the flow should be non-divergent and the thermal wind equation

must hold for both components. Hence a valid and important question is the estimation of the fields $\widetilde{u}$, $\widetilde{v}$ and $\widetilde{\rho}$, closest in some measure to the observed fields, and having a potential function $\widetilde{p}$ such that

$$f\widetilde{v} = \widetilde{p}_x/\rho_o, \tag{2a}$$

$$-f\widetilde{u} = \widetilde{p}_y/\rho_o, \tag{2b}$$

$$0 = \widetilde{p}_z - \widetilde{\rho}/\rho_o; \tag{2c}$$

the subindices denote partial derivatives and the tilde indicates the geostrophic contribution to the field. Note that providing *any* reasonable (i.e. with continuous derivatives) function $\widetilde{p}$, the system (2) can be used to define $\widetilde{u}$, $\widetilde{v}$ and $\widetilde{\rho}$, but the question posed remains incomplete until we decide which measure of closeness to optimize, which should preferably possess a precise physical meaning. A natural choice arises from the dynamical equations that describe infinitesimal amplitude internal waves. The modes described by this system on the $f-$plane (Gill, 1982), without considering boundaries, are two traveling internal waves and two static modes (i.e. modes of zero frequency). One of these last modes is a simple rearrangement of the hydrostatic, horizontally uniform background; the other corresponds to anomalies in geostrophic balance which, in the $\beta-$plane, become the low frequency Rossby wave (for example, Ripa, 1997). The energy density (Gill, 1982) for this system is a quadratic measure that can be optimized in the sense of our geostrophic estimate 'retaining most of the energy' contained in the observations. It is

$$I(\widetilde{u},\widetilde{v},\widetilde{\rho}) = \iiint [\rho_o \frac{(u-\widetilde{u})^2 + (v-\widetilde{v})^2}{2} + \frac{g^2\,(\rho-\widetilde{\rho})^2}{2\rho_o N^2}]dx\,dy\,dz, \tag{3}$$

with (2) required to hold: ρ and $\widetilde{\rho}$ are now the anomalies of density with respect to a motionless, horizontally uniform background with density $\bar{\rho} = \bar{\rho}(z)$ that defines the buoyancy frequency square, $N^2 = -g\bar{\rho}_z/\rho_o$. In other words, it is an estimate of the internal wave perturbations with the least amount of energy possible, as expressed by the measurements. The possible observation of vertical velocity is irrelevant since the geostrophic flow (f-plane dynamics) is horizontal. The study of Dickiy (1969) is more general, since it includes the effects of compressibility, but the solution given here shows explicitly why the extremum is a minimum and how the natural boundary conditions arise in irregular domains. Equation (3) is a particular choice of the weighted least-square minimization proposed by Rudnick (1996), with the ponderation arising from dynamical considerations.

The variational problem of finding an extremum of I under the constraints of system (2) can be translated into a variational problem on the single field $\widetilde{p}$, without need for Lagrange multipliers since the constraints can be included directly into the functional without further complications, giving instead of equation (3):

$$I(\tilde{p}) = \iiint \rho_o \frac{(u + \tilde{p}_y/(\rho_o f))^2 + (v - \tilde{p}_x/(\rho_o f))^2}{2} + \frac{g^2\ (\rho + \tilde{p}_z/g)^2}{2\rho_o N^2}\Big] dx\ dy\ dz. \quad (4)$$

The perspective should then be that the measurements provide information about the gradient of the single field $\tilde{p}$, from which the other fields of interest (related in system (2)) can be derived. The minimization of the functional is derived formally in Appendix A: the solution is the field $\tilde{p}$ that fulfills

$$\tilde{p}_{xx} + \tilde{p}_{yy} + f^2(\tilde{p}_z/N^2)_z = \rho_o f(v_x - u_y) - gf^2(\frac{\rho}{N^2})_z, \quad (5a)$$

with boundary conditions

$$(\tilde{p}_x,\ \tilde{p}_y,\ \tilde{p}_z) \cdot \hat{n} = (-\rho_o f v,\ \rho_o f u,\ -g\rho) \cdot \hat{n}, \quad (5b)$$

where $\hat{n}$ is a unit vector locally perpendicular to the boundary.

We now restrict the analysis, without loss of generality, to two dimensions. Equation (5a) can be easily interpreted by substituting the density anomaly with the vertical displacement of isopycnals, i.e.:

$$\rho = -\zeta \frac{d\bar{\rho}}{dz} = \zeta \frac{\rho_o N^2}{g}. \quad (6)$$

In light of (2), equation (5a) expresses

$$\tilde{v}_x - f\tilde{\zeta}_z = v_x - f\zeta_z, \quad (7)$$

which means the geostrophic estimate retains the quasi-geostrophic potential vorticity of the observed fields, a well-known property of the geostrophic adjustment problem, but not as a result of energy optimization. The linearized equations of motion establish a balance with null potential vorticity for internal waves, which are the motions that the method intends to filter out. All the results that emerge from the conservation of potential vorticity are then in agreement with a variational principle.

Vallis (1992) provides a parallel result for the shallow water equations and, for completeness, it is shown in Appendix B how the same results can be obtained for linearized dynamics without requiring Lagrange multipliers. Rudnick (1996) has proposed a more general formulation of the problem, with the optimization of a more ample quadratic measure that can be simplified into (3). Nonetheless, he decided to apply a different ponderation, mainly because the measurement errors are different for hydrography than for velocity, and other weights may give unrealistic

solutions with statically unstable density distributions, a problem that occurs in the example given in section 3, but in insignificant amounts.

One of the strengths of this method is that it gives a direct choice for the boundary condition, one that would not be straightforward if equation (5a) were derived as a result of conservation of potential vorticity. Any solution of equation (5a) with prescribed boundary conditions of the Dirichlet or Newman type (like equation (5b)) is unique and produces the minimum of equation (3), constrained to the boundary condition imposed. The direct choice is that boundary condition for which the functional (3) attains the global minimum. As deduced in Appendix A, it coincides with the so-called 'natural boundary condition' (Courant and Hilbert, 1953).

3. The example of the Yucatan Channel

A set of 15 stations spanning the Yucatan Channel were taken in 37 hours beginning on 26 May, 1997 (Fig. 1) by lowering a Sea-Bird CTD together with an RDI 300kHz ADCP. The internal recordings of the ADCP were extracted on deck between stations (Wilson, 1994). The data were interpolated by objective mapping, as described below, onto a regular grid of 1 km in the horizontal by 10 m in the vertical (1031.73 m in the horizontal by 11.28 m in the vertical, to be precise). These are shown in Figure 2.

The arithmetic mean or linear trend are removed prior to the objective mapping, although the effect is unimportant for the parameters used and the data at hand. The estimates of partial derivatives were all computed with central differences on the objective maps of the original fields. An objective mapping might use two free parameters to determine the correlation matrix. The first one defines the fraction of the variance increase due to noise, with a unit value representing the signal variance; the second parameter defines the decaying e-folding spatial scale of the correlation (i.e. the distance at which the correlation falls to e^{-1} of its initial value). The correlation function can have gaussian or, as used here, exponential decay rates, but many other correlation functions are plausible (explicit examples are shown by Chereskin and Trunnell, 1996). In a physical situation like the one pertaining to this data, where the vertical and horizontal length scales differ considerably, a third free parameter defines the aspect ratio or, equivalently, the horizontal and vertical scales are specified individually. We use a five parameter objective mapping, as described in Roemmich (1983). One pair of length scales, 80 m in the vertical and 16.5 km in the horizontal, describes the 'small' scale variability; another pair, 800 m and 165 km, describe the 'large' scale variability. A fifth parameter equal to 0.1 is retained to describe the noise variances for both scales. The Rossby radii of deformation are 44, 25, 15, and 13 km for the first four baroclinic modes, computed with respect to the sill depth (just above 2000 m). Therefore, only the first two

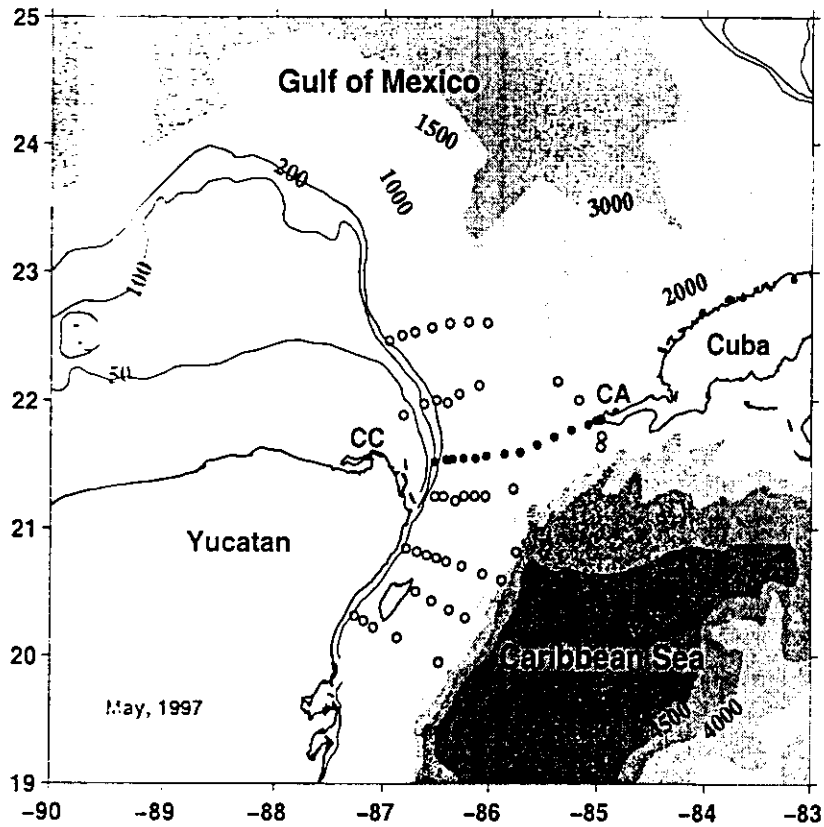

Figure 1. Distribution of stations during CANEK, with northern latitude in the abscissas and western longitude in the ordinates. The section from near Cabo Catoche (CC in Yucatan) to Cabo San Antonio (CA in Cuba) channels all the possible exchanges between the Caribbean Sea and the Gulf of Mexico. The full dots, 15 in total, mark the location of stations used in the following sections.

modes are somehow retained and the rest are damped.

The terms in the termal wind equation were used to help determine the objective mapping parameters. The mean and standard deviation of their difference change as a function of the aspect ratio of horizontal to vertical length scales. Table (1) shows some typical values of these measures, when the noise variances are kept equal to 0.1 and the vertical scales remain fixed as 80 and 800 m. Although the mean tends to decrease with the aspect ratio, the standard deviation has a minimum near an aspect ratio of 300: we use an aspect ratio of 200.

In the rest of the computations we include in the objective mappings all the profiles, a total of 33 instead of the 15 locations shown in Figure 1. For the forcing, the term due to hydrography has more 'strength' than the term $\rho_o f^2 v_x$. Their

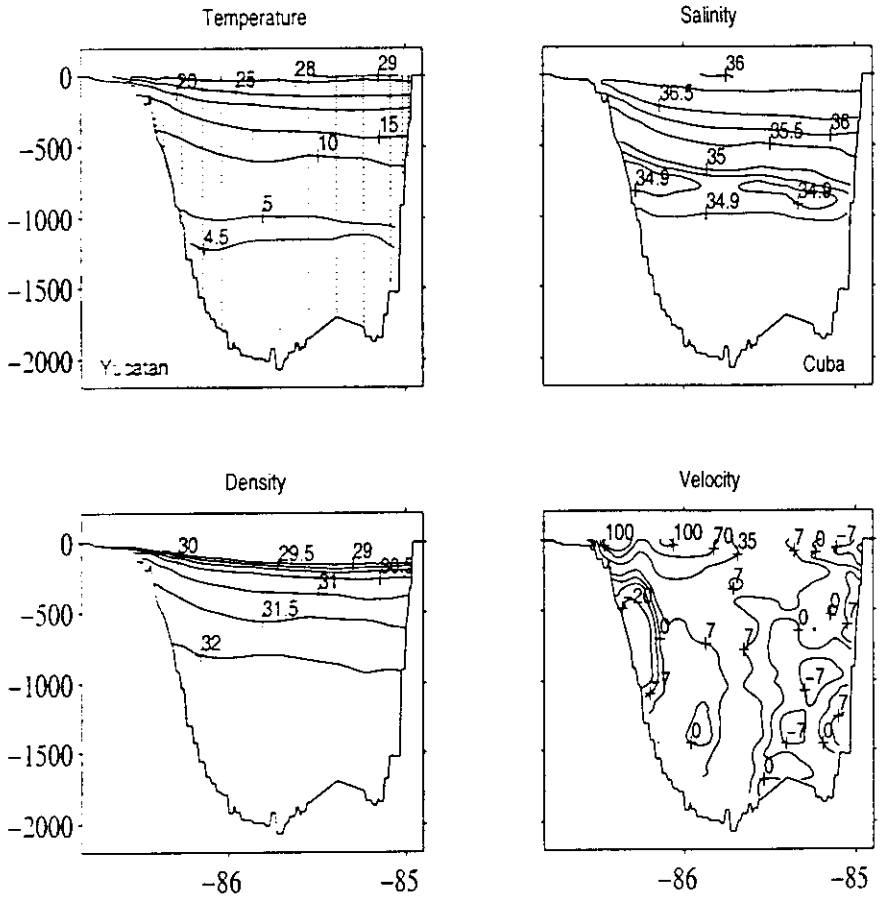

Figure 2. Distributions of temperature, salinity, density (σ_θ refered to 1000 db) and the velocity component perpendicular to the vertical section of Figure 1. The dots in the temperature map mark the data points included in the objective mapping. The axes show depth in meters in the abscissas and western longitude in the ordinates.

means are comparable, but this last term has a standard deviation about half the other (see Table (2)).

Since the purpose of the example is to show the possibilities of the method, the numerical algorithm used to solve system (5) was kept very simple, applying the grid used in the objective mapping and a standard SOR method, as described in Press *et al.* (1986, Chap. 19, Sec. 5), with the boundary aproximated as an irregular staircase closely following the bottom. The implementation of equation (5b) for horizontal or vertical boundaries is rather simple. Consider the index i along the horizontal and on a lateral boundary, with the interior towards $i-1$,

Table 1. Statistics of $-\frac{\rho_o f}{\rho_o f^2} - \frac{v_i}{f}$

Aspect Ratio	Mean	Std. Dev.
50	3.84	76.6
100	4.42	42.3
200	5.09	29.6
250	5.29	28.2
300	5.45	28.0
400	5.68	29.5
500	5.84	31.9
1000	6.21	42.1

$i - 2$, ... then a possible algorithm to update the boundary value is:

$$\tilde{p}_i = \tilde{p}_{i-1} + \rho_o f(v_i + v_{i-1})\Delta x/2. \tag{8}$$

The values at the boundary, for example v_i, are extrapolations manufactured by the objective mapping. An equivalent formula applies for derivatives when the indices represent the interior points in the vertical direction. Figure (4) shows maps of the solution gotten, as just explained, by solving Equation (5a) with a standard SOR method and Equation (8) as the implementations of Equation (5b). Table (2) provides a quantitative comparison between our geostrophic estimates and the measurements.

If we simply compute the functional (3) with $\tilde{v} = \tilde{\rho} = 0$, the average kinetic and potential energies are 32 and 36 J m^{-2} respectively. Once our estimates of $\tilde{v}$ and $\tilde{\rho}$ are used in the functional, the internal wave energies are 1 and 2, with the same order and units. The 36 J m^{-2} is indeed the available potential energy. The internal wave field has an amount equivalent to eight percent of the available potential energy. The measured transports are 29 Sv flowing into the Gulf of Mexico and 4 Sv outflowing, compared to a geostrophic estimates of 31 Sv of inflow and 5 Sv of outflow. The cross-sectional areas of inflow are 146 km^2 for the measurements and 154 km^2 for the geostrophic estimate, of a total area of 229 km^2. The inflow is slightly larger in our geostrophic estimate and in a larger area. The geostrophic estimate shows a slightly higher net transport (26 Sv) relative to the measurements (25 Sv) which is reflected in the mean velocities (item 3 in Table (2)). All these slight differences are not well resolved, given the sensitivity of the algorithm used to solve system (5).

4. Discussion and conclusions

The estimation of the geostrophically balanced fields from observed hydrographic and horizontal velocity distributions is equivalent to the geostrophic adjustment of arbitrary initial fields. The conservation of quasi-geostrophic potential vorticity

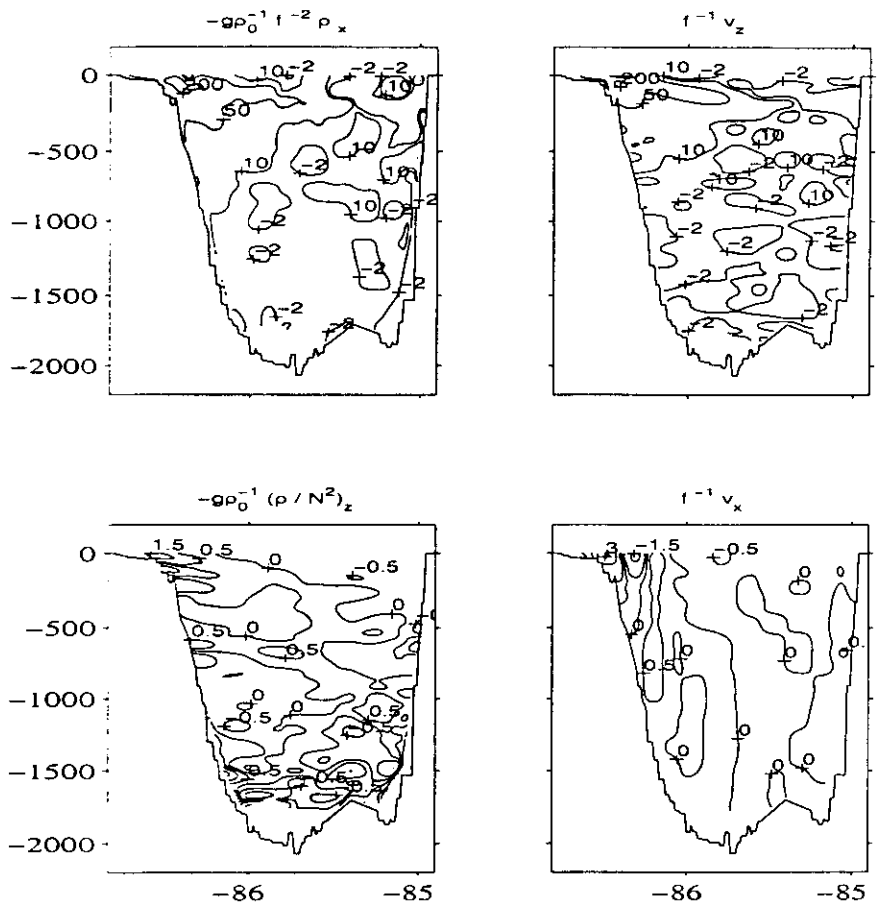

Figure 3. Distributions of the terms that balance in the termal wind equation and those that add up to the potential vorticity. The sum of the two lower maps is the forcing that defines the geostrophic pressure via equation (5a). These maps were made dimensionless with suitable normalizations, with further smoothing applied for clarity.

in the geostrophic adjustment is consistent with the a process that optimizes the 'energy retained' in the static geostrophic mode. From the available energy, a minimum amount possible is radiated away within the internal wave field (at least in its linearized version); we use quotes in 'energy retained' since the space averages of $\tilde{v}^2$ and $v^2 - v'^2$ need not be the same, since the average of vv' is not necessarily null, and similarly for the density separation in its geostrophic plus anomaly contributions. As explained by Dickiy (1969), in the geostrophic adjustment the minimum energy possible is released into the internal wave field, 'retaining' as much as possible within the geostrophic contribution.

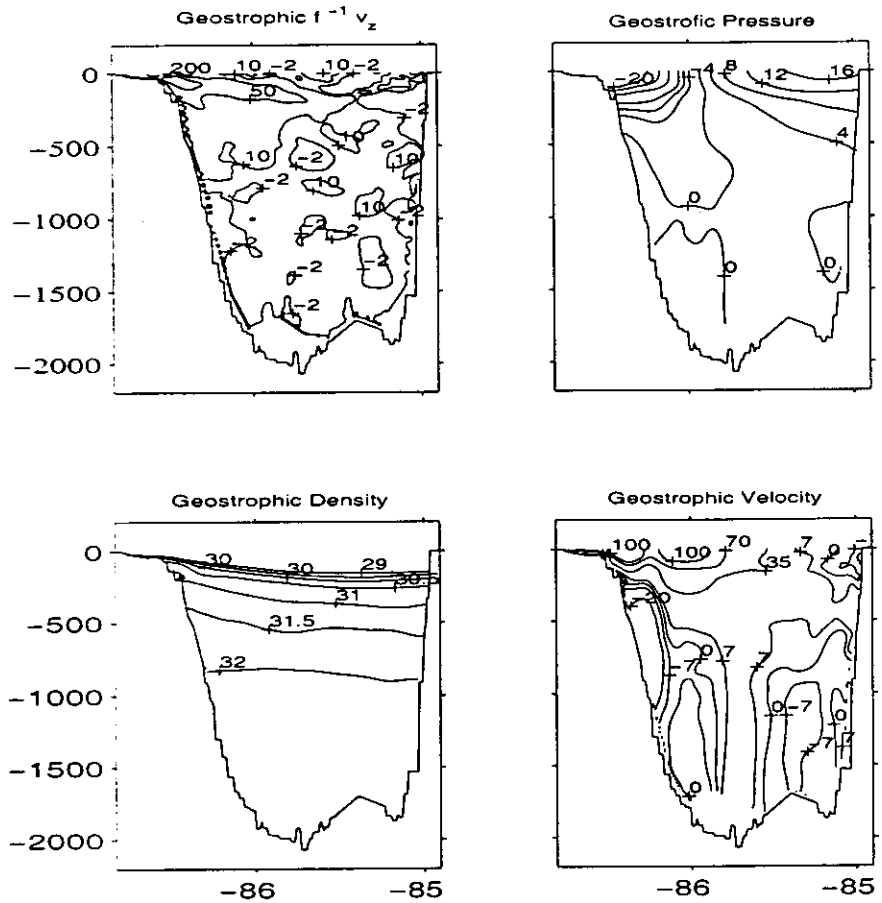

Figure 4. The upper left map shows the terms that balance in the thermal wind equation, normalized by f. The upper right map is the estimated geostrophic pressure in HPa (10^2Pa), i.e. the solution of system (5). The lower maps show the gesotrophic contributions of density and velocity, derived from the geostrophic pressure. See Figure 2 for comparison.

This method is physically sound and readily applicable. One source of contamination is any factor that introduces errors in the measured potential vorticity. These errors are fed directly into this estimate, since it is the forcing of the Poisson equation to be solved, but not all measurement errors influence the measured potential vorticity. Another source of contamination comes from the boundary conditions imposed on the Poisson equation, which are influenced by ageostrophic components.

The need to specify the boundary condition in the Poisson equation is equivalent

Table 2. Quantitative comparison of estimated and measured geostrophic fields.

	Field	Mean	Standard Deviation	Minima	Maxima	Units or factor
1	v	10.4	20.9	-21	187	cm s^{-1}
2	$\widetilde{v}$	11.0	22.2	-28	176	cm s^{-1}
3	$v - \widetilde{v}$	-.6	3.9	-11	34	cm s^{-1}
4	$\rho - \widetilde{\rho}$	-0.1	5.2	-29	45	.01 Kg m^{-3}
5	$f^{-1}(-\frac{\partial \sigma_z}{\rho_o f} - v_z)$	2.5	44.6	-652	1214	1
6	$f^{-1}(v_z - \widetilde{v}_z)$	-1.0	15	-386	273	1
7	$f^{-1}(-\frac{\partial \sigma_z}{\rho_o f} - \widetilde{v}_z)$	1.6	38	-539	828	1
8	$\frac{v_z}{f}$	0.5	29	-223	558	.01
9	$-\frac{g}{\rho_o f}(\frac{\rho}{N^2})_z$	0.5	36	-359	545	.01
10	$\frac{v_z}{f} - \frac{g}{\rho_o f}(\frac{\rho}{N^2})_z$	1	47	-363	889	.01

to the traditional problem of setting the reference velocity, an unexpected and undesired result, since this has been one of the main complications of the so-called dynamical method. One needs to realize that the geostrophic information of the measurements resides in the forcing of the Poisson equation, and such information is the derivatives of the fields, hence the need of boundary conditions. Furthermore with this method the information from hydrography comes from ρ_z and not from its horizontal derivatives, which in view of the thermal wind equation was the traditional derived field to integrate as estimate of horizontal velocities. All the diagnostic requirements of the thermal wind equations are completely fulfilled with the existence of the geostrophic pressure and that is the function this method aims to quantify.

Acknowledgments. This research was supported by CICESE, the Consejo Nacional de Ciencia y Tecnología of Mexico (CONACyT, grant 1111-2345), and the Inter-Americas Institute for Global Change (grant IAI ISP 1-084) through project *Canek: Exchange through the Yucatan Channel.* We are also grateful to the Universidad Nacional Autónoma de México for its support with shiptime and to the crew of the R/V *Justo Sierra*, captain Leobardo Ríos commanding, for their enthusiastic participation in our operations. J.L.O. wishes to acknowledge financial support from CONACyT for a sabbatical stay in the environment of RSMAS, which was made possible by the kind hospitality of Chris Mooers and very enjoyable by all the personnel of the OPEL.

APPENDIX A

Estimate of the internal wave field of minimum energy, constrained to given horizontal velocities and density distributions. We derive the requirements on the field $\tilde{p}$ for which the functional defined in equation (4) attains an extremum, which is shown to be unique and a minimum. To save space, consider the notation $a_1 = \rho_o f v$, $a_2 = -\rho_o f u$, $a_3 = -gf\rho/N$, $\tilde{p} = P$ and $I' = 2\rho_o f^2 I$, and the change of variables $x = x'$, $y = y'$ and $dz = fN^{-1}dz'$ (i.e. $z' = f^{-1}\int N dz$). Then, equivalent to equation (4), we have

$$I' = \int_{V'} N^{-1}|\vec{a} - \nabla' P|^2 dV', \tag{A.1}$$

where the integral is over the volume in transformed space ($dV' = dx'\, dy'\, dz'$), $\vec{a} = (a_1, a_2, a_3)$, and the operator $\nabla' = (\frac{\partial}{\partial x'}, \frac{\partial}{\partial y'}, \frac{\partial}{\partial z'})$. This is a problem in potential theory whose aim is to find a weighted (by $N^{-1} > 0$) least-square potential function (P) from an approximation of its gradient ($\vec{a}$). A seemingly unrealistic limitation of this formulation is the requirement of a positive definite N, but the distribution of N used can be, holding this restriction, as close to realistic profiles as desired. A straightforward evaluation of its variation (i.e. $\Delta I'(P, \delta P) = I'(P+\delta P) - I'(P)$) gives

$$\Delta I' = -2\int N^{-1}\nabla'\delta P \cdot (\vec{a} - \nabla' P)\, dV' + \int N^{-1}|\nabla'\delta P|^2\, dV', \tag{A.2}$$

from which is clear that if the first integral in the r.h.s. is null, then $\Delta I' > 0$ for all δP which are not a uniform constant. The addition of a constant to a potential function plays no role.

The use of the mathematical identity $\int \vec{B}\cdot d\vec{\sigma}' = \int \nabla'\cdot\vec{B}dV'$, where $\vec{\sigma}'$ is the surface vector locally perpendicular to the boundary and pointing outwards in the transformed coordinates, with $\vec{B} = N^{-1}\delta P(\vec{a} - \nabla' P)$, enables to write the first integral in the r.h.s of equation (A.2) as

$$\int N^{-1}\nabla'\delta P\cdot(\vec{a}-\nabla' P)dV' = \int N^{-1}\delta P(\vec{a}-\nabla' P)\cdot d\vec{\sigma}' - \int \delta P\nabla'\cdot[N^{-1}(\vec{a}-\nabla' P)]dV', \tag{A.3}$$

which is an 'integration by parts' in 3-D. Thus if

$$\nabla'\cdot[N^{-1}(\vec{a} - \nabla' P)] = 0, \tag{A.4a}$$

and

$$(\vec{a} - \nabla' P)\cdot\vec{n} = 0, \tag{A.4b}$$

where $\vec{n}$ is a vector locally perpendicular to the boundary, are fulfilled then, regardless of δP, $\Delta I'$ can not be negative and is therefore a minimum of I'. Equation

(A.4b) is known as the 'Natural Boundary Conditions' of the Poisson equation (A.4a) (see for example Courant and Hilbert, 1953). This derivation shows that the 'Natural Boundary Conditions' are required for the global minima of the functional (A.1). System (A.4) expressed in the original variables is system (5).

Appendix B

Vallis'(1992) results in the linearized dynamics without Lagrange multipliers. The typical fields used to describe a flat bottom, $f-$plane, barotropic linearized model (since anything simpler than that would hardly be of any use) are the velocity $(u,\ v)$ and the surface elevation η as functions of the horizontal position $\mathbf{r} = (x, y)$ and time, t. Its governing equations are

$$u_t \ - \ f\, v \ = \ - \ g\ \eta_x, \qquad (B.1a)$$

$$v_t \ + \ f\, u \ = \ - \ g\ \eta_y. \qquad (B.1b)$$

and

$$\eta_t \ + \ H\ (\ u_x \ + \ v_y\ ) \ = \ 0, \qquad (B.1c)$$

where H is the undisturbed thickness of the layer. Besides the two Poincaré waves there exists a static mode or geostrophic balance. The energy equation of this system relates the energy density (energy per unit area), $E = H(u^2+v^2)/2+g\eta^2/2$ with the energy flux $gH\eta(u,\ v)$, so

$$E_t \ + \ (gH\eta u)_x \ + \ (gH\eta v)_y \ = \ 0.$$

If a snapshot (i.e. $(u, v, \eta) \ = \ (u, v, \eta)(\mathbf{r}, 0)$) of the fields is known, the extremum of the 'partial energy'

$$E == \iint H\frac{(u-\widetilde{u})^2+(v-\widetilde{v})^2}{2} \ + \ g\frac{(\eta-\widetilde{\eta})^2}{2}dx\ dy, \qquad (B.2)$$

subject to the geostrophic constraints

$$-f\ \widetilde{v} \ = \ - \ g\ \widetilde{\eta}_x, \qquad (B.3a)$$

and

$$+\ f\ \widetilde{u} \ = \ - \ g\ \widetilde{\eta}_y, \qquad (B.3b)$$

separates the geostrophic contribution from the oscillatory Poincaré modes. We demonstrate this assertion below.

Given equations (B.3), the steady version of equation (B.1c) is automaticaly fulfilled by the geostrophic fields. This variational problem asks for the determination of a single field, i.e. $\widetilde{\eta}$, the constraints can be substituted directly into the

functional, and Lagrange multipliers are then not needed. As in Appendix A, we simplify the notation with $E' = 2f^2E$, $a_1 = fv$, $a_2 = -fu$, $b = g\eta$, $p = g\tilde{\eta}$ and $L = \sqrt{gH}/f$ (the Rossby radius of deformation); whence the functional can be written as

$$E' = \iint [\,|\vec{a} - \nabla p|^2 + \frac{(b-p)^2}{L^2}\,]dx\,dy, \tag{B.4}$$

from which the straightforward calculation of its variation (i.e. $\Delta E' = E'(p + \delta p) - E'(p)$) gives

$$\Delta E' = -2\iint [\nabla\delta p \cdot (\vec{a} - \nabla p) + \frac{\delta p(b-p)}{L^2} + |\nabla\delta p|^2 + \frac{\delta p^2}{L^2}]dx\,dy. \tag{B.5a}$$

Substituting the identity

$$\int \delta p(\vec{a} - \nabla p)\cdot\vec{n}dl = \iint \nabla\cdot[\delta p(\vec{a} - \nabla p)]dx\,dy,$$

where $\vec{n}$ is a unit vector locally perpendicular to the boundary and dl is the arc differential along the boundary, and using $\nabla\cdot[\delta p(\vec{a}-\nabla p)] = \nabla\delta p\cdot(\vec{a}-\nabla p) + \delta p\nabla\cdot(\vec{a} - \nabla p)$, the variation can be rewritten as:

$$\Delta E' = -2\int \delta p(\vec{a}-\nabla p)\cdot\vec{n}dl + 2\iint \delta p[\nabla\cdot(\vec{a} - \nabla p) - \frac{(b-p)}{L^2}] + |\nabla\delta p|^2 + \frac{\delta p^2}{L^2}dx\,dy. \tag{B.5b}$$

Therefore, for any δp, $\Delta E' \geq 0$ if

$$\nabla\cdot(\vec{a} - \nabla p) - (b-p)/L^2 = 0 \tag{B.6a}$$

within the domain, and

$$(\vec{a} - \nabla p)\cdot\vec{n} = 0 \tag{B.6b}$$

on the boundary. Restitution of the original notation gives

$$\nabla^2\tilde{\eta} - \frac{\tilde{\eta}}{L^2} = \frac{f}{g}(v_x - u_y) - \frac{\eta}{L^2}, \tag{B.7a}$$

and

$$\nabla\tilde{\eta}\cdot\vec{n} = fg(v, -u)\cdot\vec{n}, \tag{B.7b}$$

as the natural boundary condition. Equation (B.7a) states the conservation of linearized potential vorticity, which can be rewritten as

$$\frac{H}{f}(\tilde{v}_x - \tilde{u}_y) - \tilde{\eta} = \frac{H}{f}(v_x - u_y) - \eta,$$

and the global minimum of the functional (B.2) is reached when the natural boundary conditions apply.

REFERENCES

Cokelet, E. D., M. L. Schall and D. M. Dougherty. 1996. ADCP-referenced geostrophic circulation in the Bering Sea Basin. J. Phys. Oceanogr., *26*, 1113–1128.

Courant, R. and D. Hilbert. 1953. Methods of Mathematical Physics, Wiley-Interscience, New York. NY, 561 pp.

Chereskin, T. K. and M. Trunnell. 1996. Correlation scales, objective mapping and absolute flow in the California Current. J. Geophys. Res., *101*, 22619–22629.

Daley, R. 1991. Atmospheric Data Analaysis. Cambridge University Press, New York. 457pp.

Dikiy, L. A. 1969. A variational principle in the theory of meteorological-field adaptation. Izv. Atmos. Ocean. Phys., *5*, 188–191.

Fischer, J. and M. Visbeck. 1993. Deep velocity profiling with self-contained ADCPs. J. Atmos. Ocean. Technol., *10*, 764–773.

Fratantoni, D. M. and W. E. Johns. 1996. A Deep-Towed ADCP-CTD instrument package development for abyssal overflow measurements in the Northeastern Caribbean Sea. J. Atmos. Ocean. Technol., *13*, 680–687.

Gill, A. E. 1982. Atmosphere-Ocean Dynamics, Academic Press, London , 662 pp.

Hinrichsen, H. H. and A. Lehmann. 1995. A comparison of geostrophic velocities and profiling ADCP measurements in the Iberian basin. J. Atmos. Ocean. Technol., *12*, 901–914.

Hoskins, B. J., I. Draghici and H. C. Davis. 1978. A new look at the omega-equation. Quart. J. Roy. Meteor. Soc., *104*, 31–38.

Pinot, J. M., J. Tintoré and D. P. Wang. 1996. A study of the omega equation for diagnosing vertical motions at ocean fronts. J. Mar. Res., *54*, 239–259.

Pollard, R. T. and L. A. Regier. 1992. Vorticity and vertical circulation at an ocean front. J. Phys. Oceanogr., *22*, 609–625.

Ripa, P. M. 1997. Ondas y dinámica oceánica, *in* Contribuciones a la Oceanografía Física en México. M. F. Lavín, ed. Monografía No. 3, Unión Geofísica Mexicana, 47–74.

Roemmich, D. 1983. Optimal estimation of hydrographic station data and derived fields. J. Phys. Oceanogr., *13*, 1544–1549.

Press, W. H., S. A. Teukolsky, W. T. Vetterling and B. P. Flannery. World Wide Web sample pages from Numerical Recipes in Fortran; the art of scientific computing. Cambridge University Press. *http : //cfatab.harvard.edu/nr/bookf.html*. 1986-1992.

Rudnick, D. L. 1996. Intensive surveys of the Azores Front 2. Inferring the geostrophic and vertical velocity fields. J. Geophys. Res., *101*, 16291–16303.

Saunders, P. M. 1992. Combining hydrographic and shipborne ADCP measurements. Deep-Sea Res., *39*, 1417–1427.

Vallis G.K. 1992. Mechanisms and parametrizations of geostrophic adjustment and a variational approach to balanced flows. J. Atmos. Sci., *49*, 1144–1160.

Wilson, W. D. 1994. Deep ocean current profiling with a broad-band acoustic Doppler current profiler. Oceans'94, Proceedings, IEEE/MTS.

Wilson, W. D. and W. E. Johns. 1997. Velocity structure and transport in the Winsdward Islands Passages. Deep Sea Res., *44*, 487–520.

Wilson, W.D. and A. Leetmaa. 1988. Acoustic Doppler current profiling in the Equatorial Eastern Pacific in 1984. J. Geophys. Res., *93*, 13947–13966.

Submitted: 4 *September, 1998*